Available online at www.sciencedirect.com
ScienceDirect
Comput. Methods Appl. Mech. Engrg. 338 (2018) 41–67
Computer methods in applied mechanics and engineering
www.elsevier.com/locate/cma

Virtual elements and zero thickness interface-based approach for fracture analysis of heterogeneous materials

Matías Fernando Benedetto[a,*], Antonio Caggiano[a,b], Guillermo Etse[a,c]

[a] *Universidad de Buenos Aires, Facultad de Ingeniería, INTECIN (UBA - CONICET), Argentina*
[b] *Institut für Werkstoffe im Bauwesen, Technische Universität Darmstadt, Germany*
[c] *Universidad Nacional de Tucumán, San Miguel de Tucumán, Argentina*

Received 11 October 2017; received in revised form 21 February 2018; accepted 2 April 2018
Available online 17 April 2018

Abstract

A novel procedure for analyzing fracture processes in quasi-brittle materials and consisting in combining the discrete crack approach by means of interface elements with the Virtual Element Method is proposed and developed in this work. In particular, the proposed procedure is used in the simulation of non-linear mechanical response and cracking of cement-based composites at the mesoscopic level of observation. Thereby three components are recognized: mortar, coarse aggregates and mortar–aggregate interfaces. In this regard VEM constitutes a powerful and efficient tool to represent the complex geometries of the inclusions in composite materials, such as coarse aggregates in concrete. Actually, patches with any number of edges (not necessarily convex), hanging nodes, flat angles, collapsing nodes, etc., can be easily handled in the VEM framework while retaining the same approximation properties of FEM. On the other hand, classical zero-thickness interface elements (IEs) are employed for modeling stress-crack opening processes. A series of numerical results, not only at the mesoscopic but also at the macroscopic level of observation, are presented to demonstrate the soundness and capabilities of the proposed approach based on combinations of VEM and IEs.

Keywords: Virtual element method; Zero-thickness interfaces; Meso-scale; Fracture; Discontinuous approach

1. Introduction

Meso-scale analysis and the consideration of complex micro/meso-structural geometries in composite systems and materials has become increasingly attractive in the last years in the field of computational methods [1,2]. Plenty of computational approaches, based on the Finite Element Method (FEM), have been actually employed in several fields of solid mechanics and failure simulations [3,4].

From all possible composites considered in engineering designs and, moreover, in the field of computational solid mechanics, concrete and cementitious mixtures are amongst the most attractive ones based on the extensive use of

* Corresponding author.
E-mail addresses: mbenedet@fi.uba.ar (M.F. Benedetto), caggiano@wib.tu-darmstadt.de (A. Caggiano), getse@herrera.unt.edu.ar (G. Etse).

https://doi.org/10.1016/j.cma.2018.04.001
0045-7825/

these materials in civil constructions worldwide. In the last decades, the analysis of concrete failure and cracking behavior at the mesoscopic level of observation emerged as a promising and extremely effective technique. However, the viability and capability of meso-scale numerical tools for concrete failure analysis are deeply dependent, on the one hand, on the accuracy of the considered non-linear constitutive equations of the composite constituents and, on the other hand, they are also strongly dependent on the considered approach for modeling the interaction between these constituents [5]. Finally, and very importantly, a proper and efficient meshing of the considered micro/mesoscopic geometry and of the involved constituents is of key importance, particularly in lower scale analysis [6]. In the case of concrete composites, the constituents may include coarse and fine aggregates, cementitious mortar or paste, fibers and interfaces.

A large amount of theoretical models and numerical tools have been proposed in literature with the aim to realistically model and predict the pre- and post-cracking behavior of concrete at the meso-scale level. Some of these proposals have traditionally been implemented by means of the classical continuum-based procedures (namely, Smeared Crack Approaches — SCAs) in which the fracture zone is distributed in a certain region of the solid [7]. Other techniques follow the well-known discrete approach whereby cracks are directly represented or modeled as a jump in the kinematic field within the analyzed material [8]. Different procedures or FE techniques were proposed to materialize the discrete approach, such as the Embedded strong discontinuities (E-FEM) [9], eXtended Finite Element Method (X-FEM) [10], lattice approaches [11], particle models [12], Discrete Element Method (DEM) [13] and zero-thickness interfaces [14].

These numerical schemes incorporate meso-scale inclusions and/or heterogeneities by means of the description of a certain region of the body which has been meshed (or discretized) by using standard FEs. Nevertheless, in most cases this process becomes very difficult and inefficient when the shape, geometry and aspect ratio of the particles present high distortions and superficial tortuosity. This is one of the reasons why the majority of the available works only explicitly consider coarse aggregates but neither the medium nor the small ones [15] and, sometimes, only quite regular geometries have been handled in the scientific literature. In this regard, the Virtual Element Method (VEM) offers a very reliable and efficient alternative procedure to account for geometrically more complex inclusions and, consequently, is more suitable for arbitrary non-structured discretizations [16,17]. This issue represents one of the main advantages of the application of VEM in mesoscopic numerical analyses. In this paper, a novel and efficient procedure for numerical analysis of cracking processes in composites, characterized by geometrically complex inclusions, is proposed. It encompasses the use of two fundamental discretization strategies such as the VEM and IEs which provide relevant advantages regarding both the domain discretization and the simulation of post-cracking failure mechanisms of dissipative, brittle and quasi-brittle composites.

After the problem overview and literature review provided in this section, the paper is organized as follows: Section 2 summarizes the meso-scale approach for taking into account the composite nature of the quasi-brittle composites like concrete which are considered in this research. The basic equations and constitutive rules behind the use of zero-thickness interface elements for discrete cracking analysis are formulated subsequently, in Section 3. Afterwards, the mathematical framework and the main ingredients of the VEM applied to elasticity problems are outlined in Section 4. Some practical information behind the implementation of the proposed approach is then given in Section 5, while Section 6 deals with the numerical applications and some examples for assessing the potential and capability of the proposed approach. Some concluding remarks are finally reported in Section 7.

2. Finite element strategy for discrete failure analysis of composites with inclusions

In this section the strategy proposed in this work for discrete failure simulations of boundary value problems of composites with embedded inclusions such as the mesoscopic structure of cementitious mixtures and concrete is presented. These meso-scale structures are characterized by large aggregates embedded in mortar matrix as schematically indicated in Fig. 1.

One standard approach is to obtain a convex polygonal representation for representing the large aggregates surrounded by the mortar matrix. Traditionally, these polygons can be numerically generated through performing the so-called Voronoi/Delaunay tessellation [18] in a set of points, initially ordered in a regular array, which are slightly perturbed before the tessellation procedure as shown in Fig. 1a–b. Coarse aggregates are thus obtained by resizing and randomly rotating the Voronoi polygons as represented in Fig. 1c–d–e. The input data for the discretization procedure outlined in Fig. 1 mainly consist in the 2D specimen dimensions (based x height), mixture design parameters,

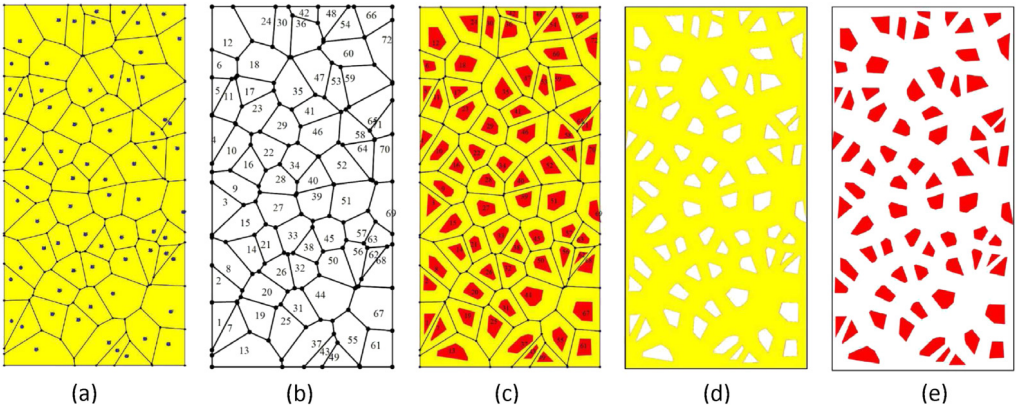

Fig. 1. Concrete meso-scale specimen 100 × 200 mm with 6 × 12 coarse aggregates: (a) random perturbed points (started from a regular array), (b) Voronoi/Delaunay tessellation, (c) meso-scale concrete specimen and (d–e) details of the meso-structure.

aggregate arrangements (i.e., coarse aggregates number in the X- and Y-direction), volume fraction and the following two geometric parameters for controlling the shape characteristics of the aggregates to be generated:

$$sp_1 = 4\pi \frac{A}{P^2} \in [0, 1] \qquad sp_2 = \frac{\min a_i}{P} \in [0, 1] \tag{1}$$

being A and P the area and perimeter of a single aggregate, respectively, while $\min a_i$ represents the minimum value of the side length of the polygon: sp_1 and sp_2 may vary from values close to one, in case of very regular inclusions (e.g. for a circle $sp_1 = sp_2 = 1$) to values close to zero for very irregular shapes, such as very stretched polygons with small length sides. sp_1 can be mainly used for avoiding stretched polygons in meso-structure representation while sp_2 for limiting polygons with small sides. The meso-structure previously presented in Fig. 1 has aggregates with 20% in volume fraction and no limits were imposed for controlling the aforementioned sp_1 and sp_2 parameters. It is worth mentioning that aggregates with high irregularities enforce very fine FE discretizations with a large number of elements. To counter this drawback, which actually could lead to unstable and very high time-consuming computational processes, critical threshold for sp_1 and sp_2 shall be fixed, thus avoiding irregular geometries (e.g., stretched polygons with small sides). Once the meso-geometry was generated, both polygonal particles and the areas between them (surrounding matrix) can be meshed with classical FEs for generating the model analysis.

This work introduces a novel alternative to this approach based on the use of VEs, which are capable of modeling complex inclusions such as those of concrete aggregates (even non convex) with few elements, aiming to overcome the aforementioned drawbacks.

For cracking simulations based on the discrete crack approach, main assumptions deal with considering the continuum elements as linear elastic while all the non-linearities are introduced into the interface elements. For this purpose, once the specimen discretization with continuum finite/virtual elements is completed, interface elements are introduced along all matrix-to-matrix solid element joints, as well as on all matrix-to-inclusion joints (more on this is fully described in Section 5). This process consists on a proper duplication of the nodes and subsequent changes in element nodal connectivities. Any nonlinearity (e.g., thermal, chemical, mechanical) is treated within zero-thickness interface elements defined throughout the adjacent edges of the meshed continuous VEs. Plenty of examples reported in the following sections will help to clarify these concepts.

3. Overview on interface elements for discrete crack analysis

This section is aimed at reviewing the most relevant proposed strategies for both interface elements and meso-scale discretizations that were considered for discrete crack-based failure analyses of cementitious composites. Additionally, the governing equations for classical zero-thickness joint elements have been summarized.

Mechanical contacts [19,20], bond mechanisms [21,22] and material discontinuities dealing with cracks and fracture evolutions in quasi-brittle materials [23,24] represent the most common and practical cases where interface elements based on zero-thickness layers have been employed in scientific literature. They are formulated in terms of

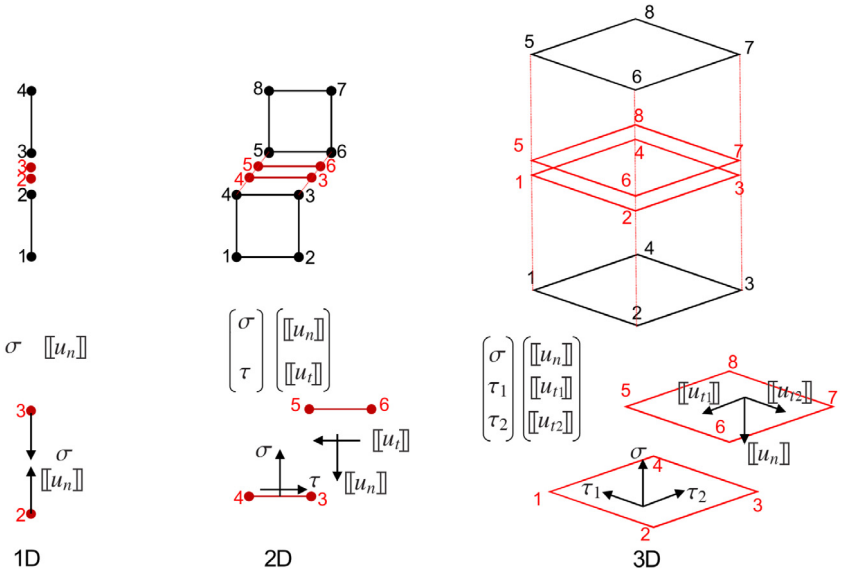

Fig. 2. Zero-thickness interface elements for 1D, 2D and 3D model analysis.

contact stresses versus relative opening displacements as schematically outlined in Fig. 2 for the cases of 1D, 2D and 3D discretization schemes.

A large amount of constitutive formulations available in the literature needed to predict failure behavior of cohesive-frictional materials such as soils, rocks and concretes [25]. The most frequent use of interface elements for modeling strong discontinuities in concrete is related to the so-called discrete crack approach in the framework of mesoscopic failure simulations. Thereby, interface elements are used to model not only the bond mechanisms in the interfaces between the different composite constituents, such as the mortar-to-aggregate joints [26], but also the failure behavior of the involved matrix such as cementitious mortar. This latter strategy was followed by López et al. [14,27] for rate independent 2D fracture analysis of concrete under combined stress states. Further extensions for 3D failure analysis and for rate- and time-dependent effects in concrete can be found in [5,28], respectively.

Recently, the interface model formulation was extended in [29] to encompass the failure behavior of fiber reinforced mortars. Also, transport phenomena in porous materials like concrete were modeled by means of zero-thickness interfaces, as can be seen in [30], where the moisture-driven diffusion is taken into account in the interface model formulation. Idiart et al. [6] used interfaces to model the fluid flow through discontinuities in the framework of coupled hydro-mechanical analysis of concrete drying shrinkage, while in [15] interfaces are used for coupled chemo-mechanical cracking processes in concrete affected by sulfate attack. Other relevant proposals on interface models for concrete subjected to multiphysical actions are those in [31,32], related to a diffusion reaction interface model for alkali silica reaction (ARS), and to a thermo-poromechanical interface model for concrete subjected to long term exposure of high temperature, respectively.

Explicit cracks in the form of strong discontinuities are also considered in computational solid mechanics based on the continuous or smeared-crack approaches. In these cases, the governing equations in terms of equilibrium conditions and the natural and essential boundary conditions, are complemented with the traction on the propagating crack surface Γ_d with the following equations:

$$\begin{cases} \sigma \mathbf{n}_d^+ & = \mathbf{t}_c^+ \\ \sigma \mathbf{n}_d^- & = \mathbf{t}_c^- \\ \mathbf{t}_c^+ & = -\mathbf{t}_c^- \end{cases} \quad \text{on } \Gamma_d \tag{2}$$

where $\mathbf{t}_c$ is the cohesive traction across the crack line Γ_d, while $\mathbf{n}_d$ is its unit normal vector. The above relationship is valid for any kind of discontinuous approach employed for discrete crack analyses. When zero-thickness interface

elements are used instead, the displacement field of the upper and lower faces of the interface element is given by

$$\mathbf{u}^+ = \mathbf{V}^{\mathbf{int}}\mathbf{U}^+,\ \mathbf{u}^- = \mathbf{V}^{\mathbf{int}}\mathbf{U}^-$$
$$[\![\mathbf{u}]\!] = \mathbf{u}^+ - \mathbf{u}^- = \mathbf{V}^{\mathbf{int}}\left(\mathbf{U}^+ - \mathbf{U}^-\right)$$

being $\mathbf{V}^{int}$ the matrix of interpolating polynomials, $\mathbf{U}^+$ and $\mathbf{U}^-$ denote the vector of nodal displacements of the upper and lower face, respectively, while $[\![\mathbf{u}]\!]$ is the displacement jump vector.

Using virtual work, the internal nodal force vector for the interface can be computed as

$$\begin{cases} \mathbf{f}^{int,+} = \displaystyle\int_{\Gamma_d} \left[\mathbf{V}^{int}\right]^T \mathbf{t}_c d\Gamma_d, \\ \mathbf{f}^{int,-} = -\displaystyle\int_{\Gamma_d} \left[\mathbf{V}^{int}\right]^T \mathbf{t}_c d\Gamma_d. \end{cases}$$

The tangent stiffness matrix of an interface element on Γ_d is given by

$$\mathbf{K}^{\mathbf{t}}_{\mathbf{int}} = \int_{\mathbf{\Gamma_d}} \left[\mathbf{V}^{\mathbf{int}}\right]^{\mathbf{T}} \mathbf{Q}\,\mathbf{C}^{\mathbf{t}}\mathbf{Q}^{\mathbf{T}}\mathbf{V}^{\mathbf{int}}\mathbf{d\Gamma_d},$$

where $\mathbf{Q}$ is the rotation matrix needed for the transformation of the nodal displacements when the local interface coordinate system differs from the global one, and $\mathbf{C}^t$ is the tangential material modular matrix relating the stress rate vector and the rate vector of relative nodal displacement jumps, which defines the evolution of the zero-thickness interface's kinematic field. Newton–Cotes integration rule is used to compute both, the linearly elastic interface stiffness (which for linear variations reduces to the trapezoidal rule), and the non-linear dissipative stiffness. The reason behind this choice is that full integration leads to highly oscillatory responses on the interfaces [33], which lead to instabilities and convergence issues.

An advantage of using interface elements is that they allow the computation of the interelement force vector [34]. However, as demonstrated in [35], interface model predictions suffer from lack of accuracy in some relevant cases. Furthermore, to avoid altering the solution it is advisable to set the interface stiffness parameters as high as possible. Some authors, see among others [36], recommend setting the stiffness higher than $10^3 E/L$ where E is Young's modulus of the material and L is a representative length of the specimen.

Convergence issues are known to appear in non-linear interface behavior, specially during post-peak regimes. Depending on the problem, severe snap back and snap-through behavior may appear and when penalty stiffness is employed to model contact, instabilities of the response due to discrete jumps in material behavior between contact and opening may ensue. During increasing monotonic loading beyond peak strength, strong localization of failure may take place in the active interfaces. Convergence rates of the interface numerical methods may become critical during strong localization processes when dense discretizations are considered and high number of non-linear interfaces are involved in the failure process. To overcome these difficulties, numerical strategies based on modified Newton, arc-length and energy control can be used as suggested in [37].

4. The virtual element method for elasticity problems

This section provides an outline of the main ideas behind VEM applied to elasticity problems. The first work introducing the Virtual Element Method to elasticity is by Brezzi et al. [38], which was followed by a generalization to handle different material models beyond linear elasticity [39], mixed formulation of the elasticity problem [40] and finite strain problems [41]. Some applications of the method have already appeared, such as linearly elastic problems [42], geomechanics [43], contact problems [44] and sub-surface flow [45,46]. As when applied to the case of general second order elliptic equations [47], the main idea of the method is to take advantage of a cleverly defined projection operator, which through the use of integration by parts allows the computation of the stiffness matrix for meshes comprised of arbitrary polyhedra without explicit knowledge of the local shape functions, other than over the polygon boundary where they are fully explicit by construction.

The classical elasticity problem in the domain $\Omega \subset \mathbb{R}^d$ $(d = 2, 3)$ is to find displacements $\mathbf{u} : \Omega \to \mathbb{R}^2$, such that

$$\begin{cases} -\operatorname{div}\boldsymbol{\sigma} = \mathbf{f} & \text{in } \Omega \\ \mathbf{u} = \mathbf{0} & \text{on } \Gamma_D \\ \boldsymbol{\sigma}\cdot\mathbf{n} = \mathbf{0} & \text{on } \Gamma_N \end{cases} \tag{3}$$

where σ is the Cauchy stress tensor, $\mathbf{f}$ is the volumetric load, Γ_D and Γ_N are the non-intersecting Dirichlet and Neumann boundaries respectively and $\mathbf{n}$ is the normal vector to the boundary. The extension to non-homogeneous boundary conditions is analogous to standard FEM and straightforward.

We assume a given constitutive law at every point $\mathbf{x}$ in the domain, i.e., $\boldsymbol{\sigma} = \boldsymbol{\sigma}(\mathbf{x}, \nabla\mathbf{u})$. This law may also consider the history of the material and recalls the 'black-box' approach present in many commercial software, in the sense that for given strains and certain state variables at a point inside an element, an algorithm is invoked that returns the corresponding stress values. In principle, evaluation of this function is external to the main program and need not be explicitly known.

The variational form of the problem is then to find an allowable displacement field $\mathbf{u}$ such that:

$$a(\mathbf{u}, \mathbf{v}) = l(\mathbf{v}) \quad \forall \mathbf{v} \in \left[\mathrm{H}^1_{\Gamma_D}(\Omega)\right]^2, \tag{4}$$

with $\mathrm{H}^{1\Gamma_D}(E)$ is the first order Sobolev space vanishing on Γ_D and

$$a(\mathbf{u}, \mathbf{v}) = \int_\Omega \boldsymbol{\sigma}(\mathbf{x}, \nabla\mathbf{v}(\mathbf{x})) : \nabla\mathbf{v}(\mathbf{x})\, \mathrm{dS} \tag{5}$$

$$l(\mathbf{v}) = \int_\Omega \mathbf{f}(\mathbf{x}) \cdot \mathbf{v}(\mathbf{x})\, \mathrm{dS}. \tag{6}$$

After the discretization of the domain into a polygonal mesh $\mathfrak{T}_h$ with parameter h of arbitrary and not necessarily convex polyhedral elements, the lowest order local space V_h^E for an element $E \in \mathfrak{T}_h$ is defined as

$$V_h^E = \left\{ \mathbf{v}_h \in \left[\mathrm{H}^1(E) \cap C^0(E)\right]^2 : \mathbf{v}_{h|\partial E} \in C^0(\partial E),\ \mathbf{v}_{h|e} \in \mathbb{P}_1(e)\ \forall e \subset \partial E,\ \Delta\mathbf{v}_h = \mathbf{0} \right\},$$

where $\mathbb{P}_1(e)$ is the polynomial space of degree 1 on e and $\mathrm{H}^1(E)$ is the first order Sobolev space on E. Basically, shape functions in a local VEM space V_h^E are known and continuous on the element boundary while unknown and harmonic in its interior, and the degrees of freedom are the vertex values as in standard FEM. The definition for three dimensional problems is a generalization of the plane case, where the local functions at each face of the three dimensional element belong to the 2D VEM space. For this work we restrain to linear elements only, although a higher-order generalization was put forward in the literature (see [48,49]). The global space is simply

$$V_h = \left\{ \mathbf{v}_h \in \left[\mathrm{H}^1_{\Gamma_D}(\Omega)\right]^2 : \mathbf{v}_h|_E \in V_h^E\ \forall E \in \mathfrak{T}_h \right\}.$$

The discrete bilinear form is defined as usual: for $\mathbf{u}_h, \mathbf{v}_h \in V_h$

$$a_h(\mathbf{u}_h, \mathbf{v}_h) = \sum_{E \in \mathfrak{T}_h} \int_E \boldsymbol{\sigma}(\mathbf{x}, \nabla\mathbf{u}_h(\mathbf{x})) : \nabla\mathbf{v}_h(\mathbf{x})\, \mathrm{dS}\,. \tag{7}$$

As we will only deal with linearly elastic materials under the hypothesis of small strains and displacements, some further decomposition of Eq. (7) can be developed. From the constitutive relation for linearly elastic materials, given by the fourth order constitutive tensor $\mathbb{C}$, we have that

$$\sigma(\mathbf{u}) = \lambda\, \mathrm{tr}(\epsilon(\mathbf{u}))\mathbf{1} + 2\mu\epsilon(\mathbf{u}), \tag{8}$$

where $\epsilon(\mathbf{u}) = \frac{1}{2}(\nabla\mathbf{u} + \nabla^T\mathbf{u})$ is the linearized strain tensor, $\mathrm{tr}(\epsilon)$ is its trace, $\mathbf{1}$ is the second order identity tensor and (λ, μ) are the Lamé parameters of the material. By replacing (8) in (7), the bilinear form becomes

$$\begin{aligned} a_h^E(\mathbf{u}_h, \mathbf{v}_h) &= 2\mu \int_E \epsilon(\mathbf{u}_h) : \epsilon(\mathbf{v}_h)\, \mathrm{dS} + \lambda \int_E \mathrm{div}(\mathbf{u}_h)\, \mathrm{div}(\mathbf{v}_h)\, \mathrm{dS} \\ &= 2\mu\Big(\underbrace{-\int_E \mathbf{u}_h \cdot\ \mathrm{div}(\epsilon(\mathbf{v}_h))\, \mathrm{dS}}_{\mathrm{I}} + \underbrace{\int_{\partial E} \mathbf{u}_h \cdot (\epsilon(\mathbf{v}_h) \cdot \mathbf{n}_E)\, \mathrm{dl}}_{\mathrm{II}} \Big) + \lambda \underbrace{\int_E \mathrm{div}(\mathbf{u}_h)\, \mathrm{div}(\mathbf{v}_h)\, \mathrm{dS}}_{\mathrm{III}}, \end{aligned}$$

where integration by parts was used to obtain the last equality. At this point the local projector operator $\Pi_E : V_h^E \to \mathbb{P}_1(E)$ is introduced. The definition and properties of the projection lie at the heart of the VEM philosophy, and the reader is referred to the available literature for a thorough treatment (mainly [38–40,50] for the concept and

definition, [48,44] for details of its computation). Π_E is defined by the following conditions:

$$\begin{cases} a_h^E(\Pi_E(\mathbf{u}_h), \mathbf{p}) = a_h^E(\mathbf{u}_h, \mathbf{p}) \quad \forall \mathbf{p} \in \mathbb{P}_1(E) & \text{(a)} \\ \dfrac{1}{N_v^E}\displaystyle\sum_{i=1}^{N_v^E} \Pi_E(\mathbf{u}_h(\boldsymbol{v}_i)) = \dfrac{1}{N_v^E}\sum_{i=1}^{N_v^E} \mathbf{u}_h(\boldsymbol{v}_i) & \text{(b)} \\ \displaystyle\sum_{i=1}^{N_v^E} \boldsymbol{v}_0 \times \Pi_E(\mathbf{u}_h(\boldsymbol{v}_i)) = \sum_{i=1}^{N_v^E} \boldsymbol{v}_0 \times \mathbf{u}_h(\boldsymbol{v}_i) & \text{(c)} \end{cases} \tag{9}$$

where ν_i, $i = 1, \ldots, N_v^E$ are the vertices of the element, while E and ν_0 are the coordinates of the barycenter. Since $\dim(\mathbb{P}_1(E)) = 6$, the same number of equations is needed to uniquely define the projection. (9a) provides only 3 equations, due to the fact that if $p \in \mathbb{P}_1(E)$ corresponded to one of the 3 infinitesimal rigid body motion in the plane, it automatically yields $0 = 0$. Therefore, conditions (9b) and (9c) must be added for the projector to be uniquely defined, since they impose equality of average nodal values and rotation between function and its projection, providing 2 and 1 additional equations respectively. Given that rigid body motions do not enter the computation of the bilinear form, other equivalent choices of equations could be made to eliminate them without changing the approximation of the strains. The projector is explicitly obtainable, since for $\mathbf{p} \in \mathbb{P}_1(E)$, all right hand side terms of (9) can be computed from the knowledge of the function at the Degrees of Freedom (DOF). Specifically, for (9a),

$$\begin{cases} \text{I} & = -\displaystyle\int_E \mathbf{u}_h \cdot \operatorname{div}(\epsilon(\mathbf{p}))\, \mathrm{dS} = 0 \\ \text{II} & = \displaystyle\int_{\partial E} \mathbf{u}_h \cdot (\epsilon(\mathbf{p}) \cdot \mathbf{n}_E)\, \mathrm{dl} \quad \text{is computable on } \partial E \\ \text{III} & = \displaystyle\int_E \operatorname{div}(\mathbf{u}_h) \operatorname{div}(\mathbf{p})\, \mathrm{dS} = -\int_E \mathbf{u}_h \cdot \nabla(\operatorname{div}(\mathbf{p}))\, \mathrm{dS} + \int_{\partial E} (\mathbf{u}_h \cdot \mathbf{n}_E)\mathbf{p}\, \mathrm{dl} \\ & = \displaystyle\int_{\partial E} (\mathbf{u}_h \cdot \mathbf{n}_E)\mathbf{p}\, \mathrm{dl} \quad \text{is computable on } \partial E \end{cases} \tag{10}$$

while (9b) and (9c) require only the value of the VEM function on vertices, precisely its DOF. At the same time, terms on the left hand side in (9) involve only polynomials and are therefore computable. A new bilinear form is defined:

$$\begin{aligned} \hat{a}_h(\mathbf{u}_h, \mathbf{v}_h) &= \sum_{E \in \tau_h} \int_E \boldsymbol{\sigma}(\mathbf{x}, \Pi_E(\nabla \mathbf{u}_h)(\mathbf{x})) : \Pi_E(\nabla \mathbf{v}_h)(\mathbf{x})\, \mathrm{dx} \\ &= \sum_{E \in \tau_h} |E| \sigma(\Pi_E(\nabla \mathbf{u}_h)) : \Pi_E(\nabla \mathbf{v}_h). \end{aligned} \tag{11}$$

Note that in general and unlike standard FEM, the local VEM spaces contain functions that are not polynomials. However, the discrete bilinear form $\hat{a}(\mathbf{u}_h, \mathbf{v}_h)$ is computed exactly when either one of the arguments is a polynomial (see above) and therefore the formulation of the element is such that it guarantees passing the patch test. For non-triangular elements (or non-tetrahedral elements in 3D), this approach may lead to spurious modes in the solution. As in the case of second order elliptic problems, a stabilization form S_h is introduced (see provided references for details). It *scales* appropriately, i.e., it takes care of the spurious modes and guarantees stability without affecting convergence and accuracy of the solution, as it is bounded above and below by constant multiples of the bilinear form $\hat{a}_h$ (which is responsible for consistency [39]). Thus, the complete global bilinear form becomes: for $\mathbf{u}_h, \mathbf{v}_h \in V_h$,

$$a_h(\mathbf{u}_h, \mathbf{v}_h) = \hat{a}_h(\mathbf{u}_h, \mathbf{v}_h) + \tau_h(\mathbf{u}_h) S_h(\mathbf{u}_h, \mathbf{v}_h) \tag{12}$$

where $\tau_h > 0$ is a parameter depending on the material model and the current state, and is required to adjust the stabilization term.

For the linear form corresponding to the loading term, the approximation relies on taking the average of $\mathbf{f}$ over an element with N_v^E vertices and a quadrature rule based on vertex values for the VEM function $\mathbf{v}_h$. Namely,

$$l(\mathbf{v}_h) = \sum_{E \in \mathfrak{T}_h} \mathbf{f}^E \overline{\mathbf{v}_h}^E, \tag{13}$$

where $\mathbf{f}^E = \frac{1}{|E|}\int_E \mathbf{f}\,\mathrm{dx}$, $\overline{\mathbf{v_h}}^E = \frac{1}{N_v^E}\sum_{i=1}^{N_v^E}\mathbf{v_h}(\boldsymbol{v}_i)$, although any other approximation of the loading term with the correct approximation order can be used instead of this one (e.g., using the orthogonal L^2 projection on a polynomial space) as long as it can be computed only from the values of the DOF of $\mathbf{v}_h$. The stabilization parameter for the linearly elastic case can be taken simply as $\tau_h = \lambda + 2\mu$, although for severely deformed elements with large aspect ratios some other choices have been suggested [43]. For a verification of the value for the parameter for nearly incompressible materials and non linear behavior see [50]. To summarize, the idea behind the VEM formulation is to use the projector to find a patch-test satisfying approximation of the strain field associated with a VEM shape function using constant strain values for each strain component. For this reason, the lowest order VEM discretization for elasticity has convergence properties analogous to the classical CST (constant strain triangle) element [38]. However, VEM has been shown to be less sensitive to mesh distortion [49], which along with the use of arbitrary polyhedral elements, provides greater meshing versatility. This feature makes use of VEM a very attractive approach for complex and irregular meshes such as those characterizing mesoscopic length scales of cementitious composites such as concrete and mortar, as proposed in this work.

5. Discretization and implementation of meso-scale simulations with virtual and interface elements

The discretization and cracking simulation of concrete composites based on interfaces was, since the first non-linear analysis of concrete components based on discrete crack approach, the most extensively considered strategy. Its main advantage is the inherent simplicity of its constitutive formulation and numerical implementation. The drawback of the direct procedure based on interfaces is the imposed fix crack path which may suppress the cracking evolution through other more critical paths, see a.o. [51,52]. Therefore, sufficiently dense meshes with interfaces in all solid element connections shall be considered. This section reports the geometric generation, meshing and interface addition in mesoscopic elements modeled with VEs and IEs.

5.1. Mesh generation and aggregate selection

Polyhedral meshes were obtained using Polymesher [53], a random mesh-generator algorithm for Matlab, which is based on Voronoi diagrams from random initial points called seeds. For this work, slight modifications were introduced in the code to allow for some bias in the random selection of the element seeds. The initial polyhedral mesh is usually rough and uneven, and through several iterations uniformity is obtained, converging to a very regular hexagonal mesh. In some of the numerical studies presented in this paper, a rougher, more irregular mesh was chosen to better model the unevenness of actual concrete samples (as in Section 6.2.3), while in others more iterations of the mesh were performed for a smoother representation of the geometry (e.g. the debonding problem of Section 6.2.2). Throughout this work, element coloring in the shown meshes indicates the number of vertices of the element.

Meso-scale simulations of heterogeneous materials should geometrically represent the different constituents and their most relevant properties. When using triangular elements in meso-scopic discretizations, some relevant difficulties may appear such as the presence of small angles and edges, bad aspect ratios and low-quality elements in general. These complications can be avoided using arbitrary polyhedral elements that do not require any further discretizations between aggregates and, therefore, do not lead to the aforementioned mesh defects. Since meshing complex aggregate geometry is no longer needed, there will be an improvement in element quality.

In order to represent different material properties of heterogeneous media we propose an approach that takes advantage of discretizing the domain into arbitrary virtual elements. In a given polyhedral mesh, the ratio p of aggregate volume to total volume is set. In the numerical results for heterogeneous concrete-like materials in Sections 6.2.3 and 6.2.4, a new randomly generated mesh is produced at the start of each simulation, whose aggregate selection is also randomly obtained. Due to this latter fact, the results of the analysis vary within a certain range depending on discretization parameters such as maximum element size and shape, aggregate density and distribution, and material features. The limitation for selecting aggregates is that they are not in contact with the boundary nor with other aggregates. Voids in the specimen can be inserted analogously.

Finally, whenever independently obtained meshes need to be compatibilized (as in several of the problems presented in Section 6), full advantage is taken from VEM features to deal with hanging nodes. In this way, different meshes merge into a globally conforming mesh by sharing all nodes on the common boundary.

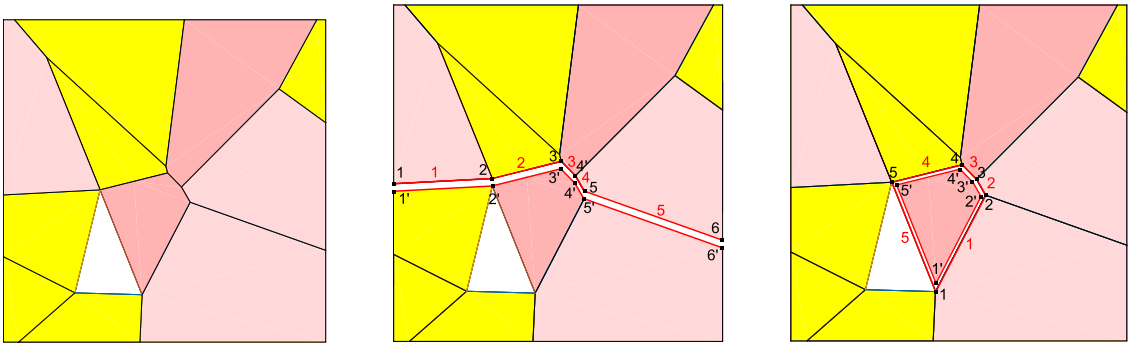

(a) Original mesh. (b) Closed path. (c) Surrounding an element.

Fig. 3. Inserting interface elements into a virtual element mesh.

5.2. *Interface elements addition*

Traditional IEs are added on edges of the VE mesh. These interfaces can be introduced regardless of the shape of the VE, and since the functions in the local VEM spaces are polynomials on the boundaries of the element (Section 4), the insertion of IEs provided the polynomial degree in the interface and the VEM discretization order agree) is the same as with standard FEM. It is not possible however to introduce IEs that do not form a closed path on the mesh, since that would result in a physically inconsistent non-propagating crack path. Therefore, two procedures for inserting interface elements are applied. The first one deals with closed paths (as in Sections 6.1.1, 6.1.2 and the debonding test in 6.2.2), in which interfaces are added following the path until the last interface finishes either at the beginning of the first interface or at the boundary. In the latter case, it is required that the interface also begins at the boundary. This approach allows to introduce the minimum required amount of IEs to follow the crack path, although it requires a priori knowledge of the path. The second approach allows inserting IEs surrounding any element, and therefore a closed loop is always determined. This becomes specially useful when one needs to surround a particular element with interfaces (e.g., an aggregate in a cement matrix), since the process is done locally on the element. It is also much more practical in the case of interface elements in all possible inter-element boundaries. Fig. 3 illustrates both alternatives described here, showing node duplication and interface creation.

5.3. *Interface constitutive rules*

The stress-opening responses and the cracking separations of the interface elements analyzed in Section 6 have been formulated in terms of 2D normal/shear stress components, (σ, τ), related to the corresponding jump in displacements, $[\![\mathbf{u}]\!] = ([\![u_n]\!], [\![u_t]\!])$. Specifically, the following interface-rules have been employed:

- A linear elastic relationship for the analysis of the plate with a circular inclusion in Section 6.1.1.
- A cohesive zone model proposed by Tvergaard [54] for the analysis of the peeling test in Section 6.1.2.
- The fracture-based rule proposed by Park et al. [55] for all mesoscale analyses outlined in Section 6.2.

The detailed description of the models are documented in the corresponding Sections.

6. Numerical results

The aim of this section is to report the importance of polygonal VEM meshing and approximation in practical cases as presented below, showcasing the capabilities, numerical efficiency and resolution of the proposed approach based on the combination between VEM and IEs. Results are presented, beginning with benchmark problems followed by applications for meso-scale systems. All numerical results were obtained using an in-house code in the MATLAB programming language. In non-linear problems, the incremental-iterative solution was obtained with a standard Newton-type method under displacement control, with additional care to ensure convergence (e.g., smaller load steps,

adjusting tolerances). At each load and/or displacement increment, the tangent stiffness matrix is computed and the solution is updated until equilibrium is achieved. Since bulk elements are always linear elastic and non-linearities are only present on the interfaces, the tangent stiffness matrix of the VEs is trivial and for the IEs it can be analytically computed beforehand and evaluated accordingly. The ill-conditioning of certain problems involving fracture behavior suggests the use of more advanced tools such as line search, arc-length, and energy based methods, [56], to ensure proper convergence, although all results presented in the following were obtained with the standard method.

6.1. Benchmark problems

6.1.1. Linear elastic plate with circular inclusion.

As first example, a plate with a circular inclusion is put forward so as to highlight some of the capabilities of the VEM for seamlessly integrating non matching meshes in order to include interface elements between different materials. In this context, similar analyses of such systems (i.e., a medium with inclusions) were performed in former communications in scientific literature [41,39,57,58].

The BVP involves two linearly elastic materials for the plate and a circular inclusion. Problem geometry and a detail of the plate-to-inclusion interface is presented in Fig. 4. The element colors in the picture on the left hand side of this Figure indicates number of edges of the element while the picture on the right shows the different material properties considered in the analysis. A quarter of the mesh was generated and replicated using symmetry to obtain the final mesh, as well as a grading criteria to obtain a finer mesh around the inclusion. Since both components were meshed independently, there was no mesh conformity requirement. As explained in Section 5.1, this poses no problem for the VEM, and it is handled by sharing nodes on the interface and defining collinear adjacent edges so that no gaps in the mesh are left.

The plate length is 2 mm, Young's modules are $E_p = 50$ MPa and $E_i = 25$ MPa for the plate and the inclusion respectively, Poisson's ratio for both materials was set as $\nu_p = \nu_i = 0.25$ and a far field stress of $\sigma_x = 1$ MPa is imposed. The boundary conditions consist of fixing the vertical displacement for nodes (0, 1) and (2, 1) and the horizontal displacement for nodes at (1, 0) and (1, 2), which is more than enough to eliminate rigid motions and with no reaction forces present due to the symmetry of the applied load. An analysis of this problem with analytical solutions in the context of numerical manifold method can be found [59], and a comparison of the obtained results will be made with the solution provided there. Assuming, as in this case, that the Lamé parameters λ_p, μ_p and λ_i, μ_i for the plate and inclusion respectively satisfy $\lambda_p = \mu_p$ and $\lambda_i = \mu_i$, then the analytical solution of the linearly elastic problem of an infinite plate with an inclusion in polar coordinates is given by

$$\sigma_r = \begin{cases} \dfrac{3\mu_i\sigma_x\cos^2(\theta)}{\mu_p + 2\mu_i} & r \le a \\ \dfrac{\sigma_x\left(r^2\left(a^2(\mu_i-\mu_p)+r^2(\mu_p+2\mu_i)\right)+\cos(2\theta)\left(3a^4(\mu_p-\mu_i)+4a^2r^2(\mu_i-\mu_p)+r^4(\mu_p+2\mu_i)\right)\right)}{2r^4(\mu_p+2\mu_i)} & r > a \end{cases}$$

$$\sigma_{r\theta} = \begin{cases} -\dfrac{3\mu_i\sigma_x\sin(\theta)\cos(\theta)}{\mu_p + 2\mu_i} & r \le a \\ -\dfrac{\sigma_x\sin(2\theta)\left(a^4(\mu_i-\mu_p)+2a^2r^2(\mu_p-\mu_i)+r^4(\mu_p+2\mu_i)\right)}{2r^4(\mu_p+2\mu_i)} & r > a \end{cases}$$

$$\sigma_{\theta\theta} = \begin{cases} \dfrac{3\mu_i\sigma_x\sin^2(\theta)}{\mu_p + 2\mu_i} & r \le a \\ -\dfrac{\sigma_x\left(\cos(2\theta)\left(3a^4(\mu_p-\mu_i)+r^4(\mu_p+2\mu_i)\right)-r^2\left(a^2(\mu_p-\mu_i)+r^2(\mu_p+2\mu_i)\right)\right)}{2r^4(\mu_p+2\mu_i)} & r > a \end{cases}$$

where a is the radius of the inclusion and the origin of coordinates is located at the center of the inclusion.

Using a very fine mesh made up of 8000 polygonal elements, a reference solution was obtained (Fig. 5), where the unsmoothed values of σ_x on the vertical mid section and on the interface were 0.7496 and 1.4810 for the inclusion and the plate respectively. A very good agreement is therefore found with the analytical values of 0.75 MPa and 1.5 MPa, considering that the plate is not infinite, the lowest order virtual elements have a constant stress approximation within the element and we are comparing a value on the interface with one which is constant on the whole element whose barycenter does not lie on the interface.

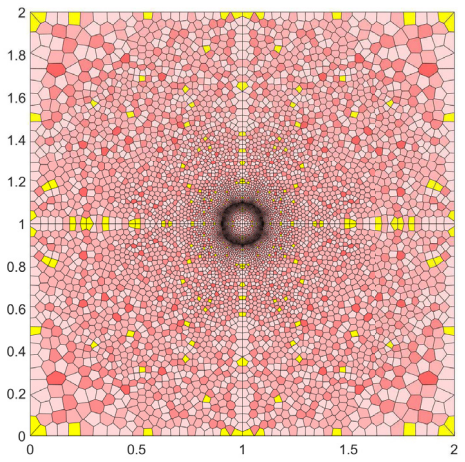

(a) Geometry and virtual element mesh.

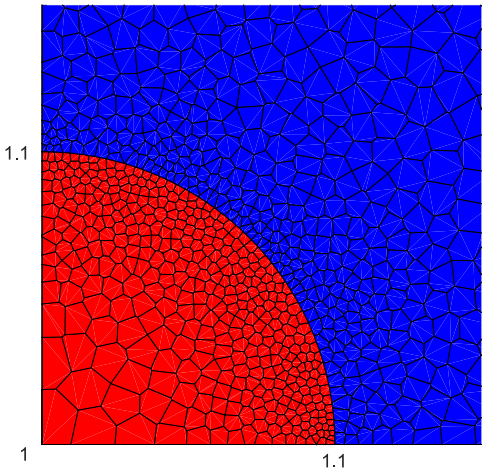

(b) Detail of mesh non-conformity between plate and inclusion (inclusion mesh is roughly twice as fine).

Fig. 4. A linearly elastic benchmark: Geometry and mesh. (For interpretation of the references to color in this figure legend, the reader is referred to the web version of this article.)

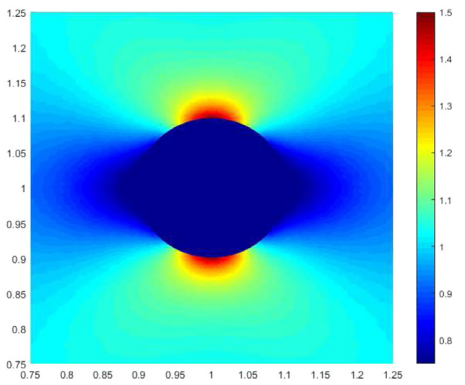

(a) Smoothed stress field σ_x.

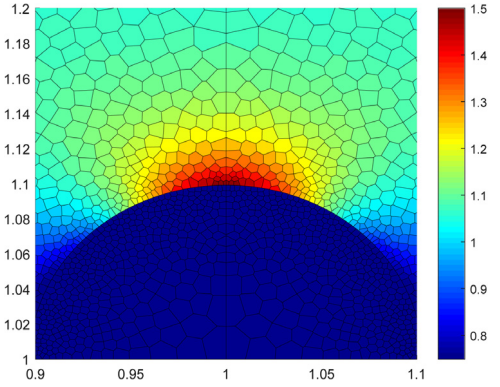

(b) Unsmoothed stress field σ_x around inclusion.

Fig. 5. A linearly elastic benchmark: Results for σ_x (MPa).

We now introduce a new mesh with the same discretization but with the addition of IEs, depicted in blue as shown in Fig. 6(a). The goal is to determine a value for the tangential K_t and normal K_n stiffness of the linear interface elements that preserves the accuracy of the solution. By considering $K_t = K_n = 10^n E_p$ and gradually increasing the value of n in all interface elements, a comparison is made with the reference solution (i.e., continuum elements with no interface between them). Fig. 7(a) shows the results of the stress profile σ_x along the vertical symmetry axis ($x = 1$) for increasing values of the stiffness parameters of the interfaces, including the reference and the analytical solution. Due to symmetry, only the upper half of the problem geometry is shown. The integral of the stress profile along $x = 1$ is selected as a quantification of the influence of the interface stiffness. The relative error of the integral of σ_x along the vertical symmetry axis, i.e. $\int |\sigma_{x,REF} - \sigma_{x,n}| dy / \int |\sigma_{x,REF}| dy$ is shown in Fig. 7(b). From these results it can concluded that for $n \geq 3$ the influence of the interface elements is negligible. Even for $n = 2$, i.e., an interface 100 times stiffer than the plate, the influence can be barely appreciated. Lower values of n show a noticeable effect which is of course dependent on the geometry of the mesh.

The final results for this section deal with the possibility of computing interface stresses. In order to obtain accurate results some weight parameters need to be considered, as explained in [35], whereby a different stiffness is assigned

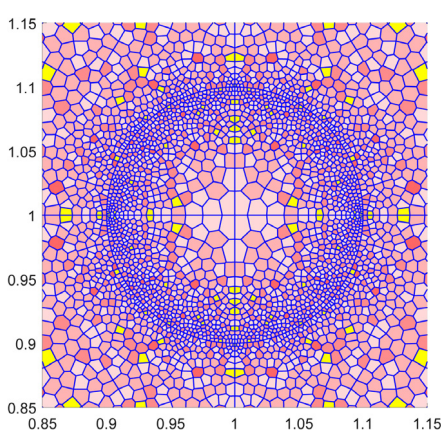

(a) Mesh with interface elements on all mesh edges.

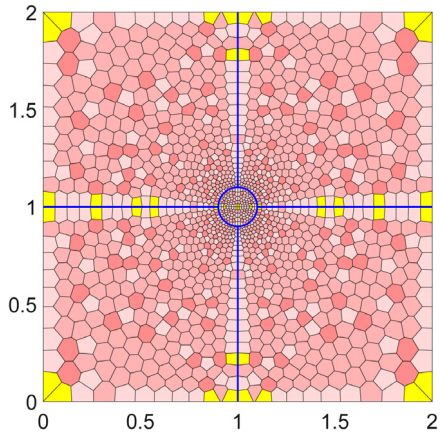

(b) Mesh with interface elements only on interface and symmetry axes.

Fig. 6. A linearly elastic benchmark: Addition of interface elements. (For interpretation of the references to color in this figure legend, the reader is referred to the web version of this article.)

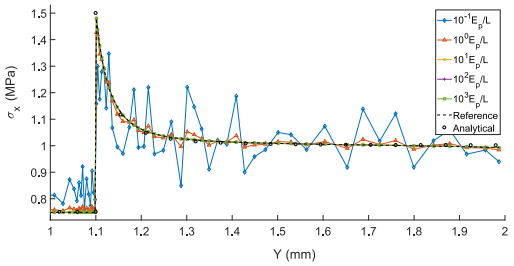

(a) Comparison of computed values of σ_x.

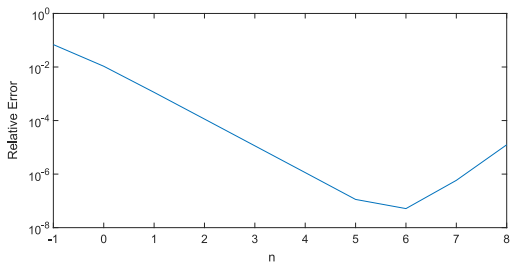

(b) Relative error of the stress profile σ_x on the line $x = 1$.

Fig. 7. Results for stress field σ_x on $x = 1$.

to the end nodes of an interface depending on the number of interfaces converging to each pair of nodes and their relative orientation. Interface lines will be introduced along the vertical and horizontal symmetry edges, as well as on the plate/inclusion interface, as shown in blue in Fig. 6(b). Since penalty stiffness values are non unitary only in intersections of 3 or more interfaces, it was only required to compute them on the 4 locations where the symmetry axis meet the border of the inclusion. Results for normal and tangential interface stresses are shown in Figs. 8 and 9, where the obtained solution (marked with circles) is plotted from different viewpoints together with the corresponding analytical solution. The provided dashed lines represent the boundaries of the plate and the inclusion.

Some conclusions arising from these results are that good agreement is found between the computed and the analytical solutions regarding both normal and tangential stresses. This is remarkable given that the problem was discretized with arbitrary VEM polygonal elements of the lowest order, the Newton–Cotes approximate integration rule was used and there is no conformity requirement whatsoever between mesh for the inclusion and for the plate. Additional experimental results with full integration on the interface elements and without penalty parameters resulted in higher oscillations and were, consequently, less representative of the real solution (not shown).

6.1.2. Peeling test

In this section a type of bond-slip test is analyzed. Namely, the separation of two layers which are connected by an interface. This problem was studied in [60] in the context of node-to-segment interface elements.

As the lower layer is much stiffer than the upper one, very small deformations are expected in the lower one and therefore it seems reasonable to use a coarse mesh for that part of the problem. However, in order to accurately

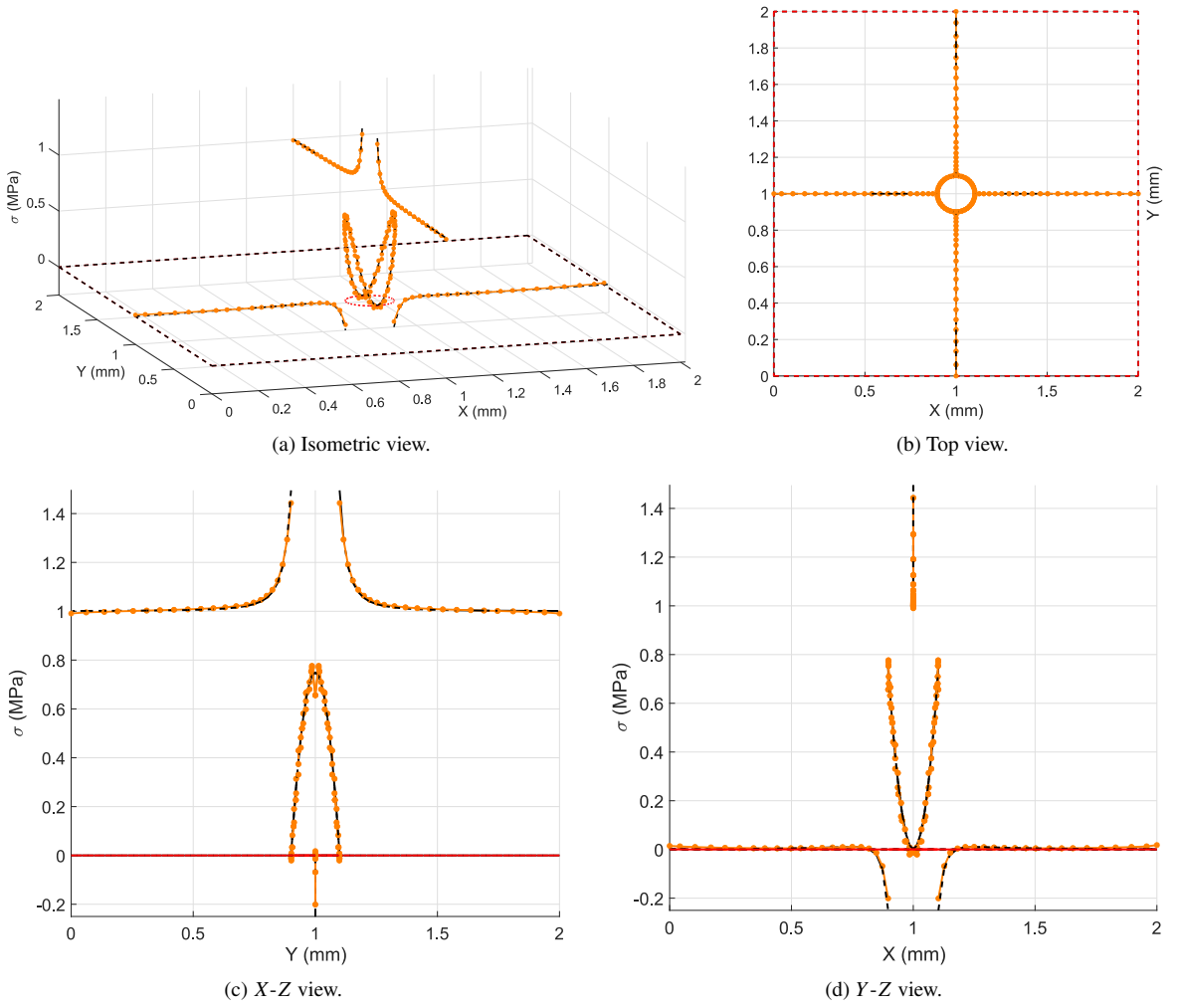

(a) Isometric view.

(b) Top view.

(c) X-Z view.

(d) Y-Z view.

Fig. 8. Values of analytical and computed normal interface stresses.

represent the deformation that the peeled layer undergoes, it is advisable to provide a sufficiently fine discretization of that layer as well. Taking advantage of the versatility of the VEM, the lower substrate can be discretized differently by using arbitrary polygons that can interact with any number of IEs used to model the connection between both substrates. In this way non-matching meshes are introduced, with varying mesh sizes and without the need for any special treatment nor sacrificing accuracy The interface constitutive model used for this test was introduced in [54], and here presented for completeness. For relative normal and tangential displacements Δ_n and Δ_t, the corresponding normal and tangential stresses are given by

$$\sigma = \frac{27}{4}\sigma_{max}\frac{\Delta_n}{\delta_{nc}}(1-2\lambda+\lambda^2)$$
$$\tau = \frac{27}{4}\tau_{max}\frac{\Delta_t}{\delta_{tc}}(1-2\lambda+\lambda^2)$$

where σ_{max} and τ_{max} are the maximum stresses, δ_{nc} and δ_{tc} are the critical openings, and λ is a dimensionless parameter called effective displacement, defined as $\lambda = \sqrt{(\frac{\Delta_n}{\delta_{nc}})^2 + (\frac{\Delta_t}{\delta_{tc}})^2}$. For $0 \leq \lambda$ and $1 \leq \lambda$, i.e., for no relative displacement or relative displacement exceeding critical openings, we have $\sigma = \tau = 0$. When normal stresses are negative (i.e., there is compression at the interface) a penalization was applied thereby increasing stiffness in order

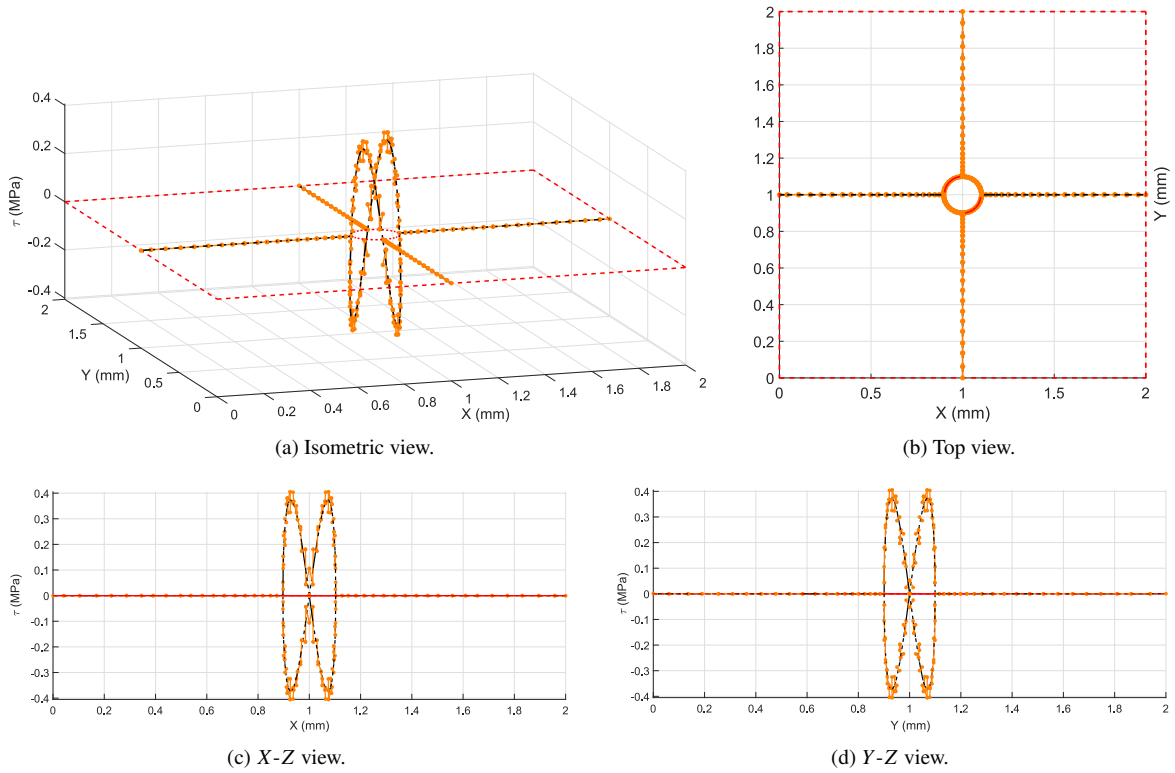

(a) Isometric view.

(b) Top view.

(c) X-Z view.

(d) Y-Z view.

Fig. 9. Values of analytical and computed tangential interface stresses.

Table 1
Data for the peeling test.

σ_{max}	τ_{max}	δ_{nc}	δ_{tc}	E_{top}	ν_{top}	E_{bottom}	ν_{bottom}
30 MPa	30 MPa	0.1 m	0.1 m	10^5 Pa	0	10^{10} Pa	0

to avoid interpenetration and to appropriately model the contact constraint. Material parameters for this problem are given in Table 1.

The geometry of the problem as well the boundary conditions are shown in Fig. 10, where the 4 different meshes under consideration are presented. Once again, element coloring indicates the number of edges for each element. Table 2 summarizes mesh composition and discretization, where Bx, By, Tx and Ty indicate number of elements for the bottom and top substrates respectively, in the x and y directions. Note that Mesh A is regular rectangular conforming mesh, while the others include elements with more than 4 edges. In particular, Mesh C presents no common node between substrates in the interior of the interface while Mesh D uses a single 27 sided element for the discretization of the lower substrate. Loading F is applied through small displacement increments in the upper right corner, until the final vertical displacement $\delta = 0.1$ m is reached.

Results comparison for different meshes is based on the applied force and the interface normal stress. In Fig. 11(a) the final solution is shown for Mesh D. Results for normal stresses along the interface are shown in Fig. 11(b), where a maximum value close to σ_{max} is attained near $x = 0.6$ m in all cases. As the vertical displacement approaches the critical normal opening, the interface is expected to become more compliant and the force needed to impose the displacement increment should be reduced. That is indeed the case, and values of the applied force show a very good agreement for all meshes (Fig. 11(c)). Practically the same values of F were obtained for meshes A, B and D, while a very slight difference is appreciated for mesh C, explained by the different number and distribution of the IEs. From the results of this benchmark test it can be concluded that differences in the results from using different

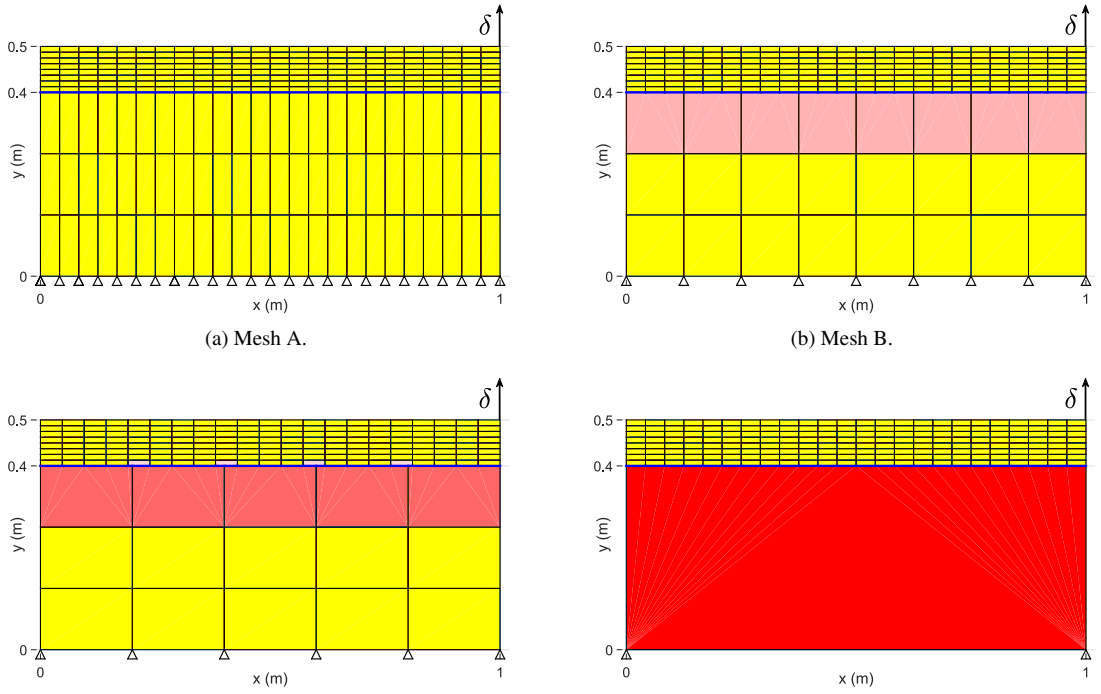

(a) Mesh A. (b) Mesh B.

(c) Mesh C. (d) Mesh D.

Fig. 10. Geometry, meshes, and boundary conditions for Peeling test.

discretizations were negligible which demonstrates the objectivity of the interface numerical predictions regarding composition, conformity and coarseness of the considered discretizations.

6.2. Mesoscopic numerical analyses

In this section, finite element discretizations composed by VEM and IEs as described in previous sections are considered for analyzing deformation and failure problems of composite materials at the mesoscopic level of observation. The traction-separation law used for the IEs is described in the following, while the bulk is, in all cases, a linearly elastic material. We begin with two classic analysis of a fiber composite before introducing uniaxial tests and a three point beam problem more related to meso-scale simulations of a concrete-like material.

6.2.1. Cohesive constitutive model for the interface

The interface elements for the numerical simulations presented in the following (Section 6.2) obey a material behavior based on a potential proposed in [55,61] for defining the traction separation law in a Cohesive zone model (CZM). Normal and tangential stress (σ and τ) are defined in terms of the relative openings Δ_n and Δ_t and depend on 8 parameters:

Parameter	Description	Unit
σ_{max} τ_{max}	Critical interface stresses	MPa
ϕ_n ϕ_t	Energies for pure fracture modes I and II	N/mm
α β	Post-peak softening behaviors	–
λ_n λ_t	Ratios between final and critical opening	–

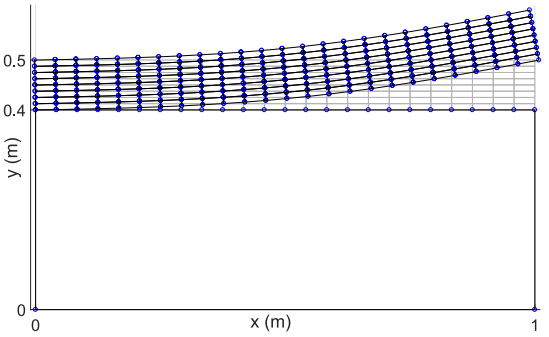

(a) Final geometry.

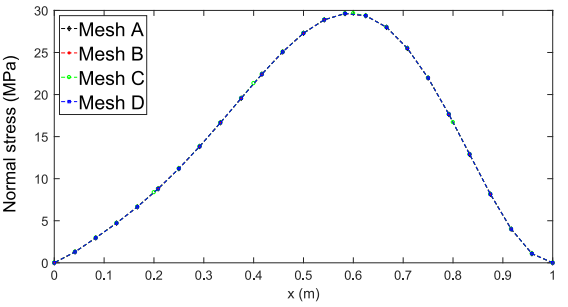

(b) Normal stress along the interface at final state.

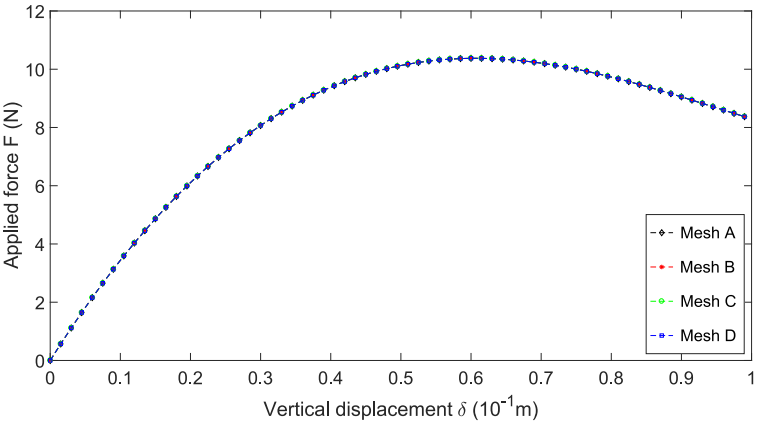

(c) Applied force.

Fig. 11. Results for peeling test.

Table 2
Mesh composition for peeling test.

Mesh	Bx	By	Tx	Ty	Total VEs	IEs
A	24	3	24	8	264	24
B	8	3	24	8	216	24
C	5	3	24	8	207	28
D	1	1	24	8	193	24

Explicit formulas for interface stresses are:

$$\sigma = \frac{\Gamma_n}{\delta_{nf}}\left[p\left(1-\frac{\Delta_n}{\delta_{nf}}\right)^{\alpha}\left(\frac{\Delta_n}{\delta_{nf}}+\frac{p}{\alpha}\right)^{p-1} - \alpha\left(1-\frac{\Delta_n}{\delta_{nf}}\right)^{\alpha-1}\left(\frac{\Delta_n}{\delta_{nf}}+\frac{p}{\alpha}\right)^{p}\right]$$
$$\times\left[\Gamma_t\left(1-\frac{|\Delta_t|}{\delta_{tf}}\right)^{\beta}\left(\frac{q}{\beta}+\frac{|\Delta_t|}{\delta_{tf}}\right)^{q}+\max(0,\phi_t-\phi_n)\right]$$
$$\tau = \frac{\Delta_t\Gamma_t}{|\Delta_t|\,\delta_{tf}}\left[q\left(1-\frac{|\Delta_t|}{\delta_{tf}}\right)^{\beta}\left(\frac{|\Delta_t|}{\delta_{tf}}+\frac{q}{\beta}\right)^{q-1} - \beta\left(1-\frac{|\Delta_t|}{\delta_{tf}}\right)^{\beta-1}\left(\frac{|\Delta_t|}{\delta_{tf}}+\frac{q}{\beta}\right)^{q}\right]$$
$$\times\left[\Gamma_n\left(1-\frac{\Delta_n}{\delta_{nf}}\right)^{\alpha}\left(\frac{p}{\alpha}+\frac{\Delta_n}{\delta_{nf}}\right)^{p}+\max(0,\phi_n-\phi_t)\right]$$

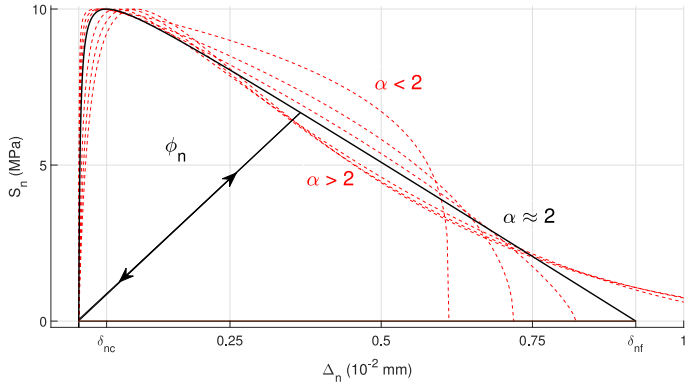

(a) Interface shear strength variation under pure extension displacement.

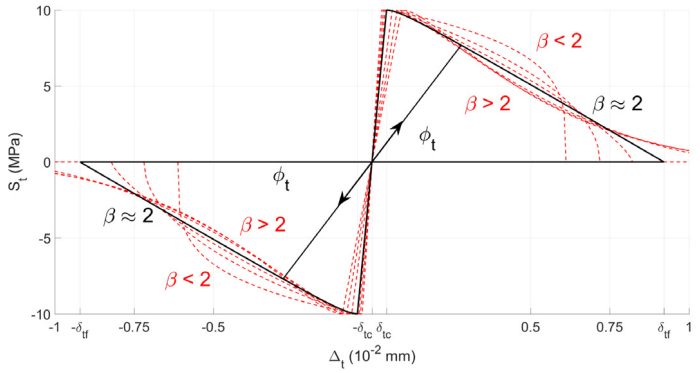

(b) Interface shear strength variation under pure lateral displacement.

Fig. 12. Traction separation law in pure modes.

where δ_{nf} and δ_{tf} are the final normal and tangential openings respectively, which establish the limit for the available interface stiffness, and δ_{nc} and δ_{tc} represent the normal and tangential critical opening, respectively, for peak interface strength. Γ_n and Γ_t are two constants which are related to the fracture energy values and can be easily evaluated by following the energy principles of the model while p and q are non-dimensional exponents whose expressions are given in terms of the ratios between the final and critical opening (λ_n and λ_t) and in terms of the parameters α and β. The model does not account for friction originated from crack closure, which can be relevant in cohesive-frictional materials with aggregates (as in [62,63]).

In the intrinsic approach, interfaces are provided with a high initial stiffness until the critical stress is reached and are usually simplified as linear until the peak, where the behavior changes abruptly. The model used in this work incorporates a smoothly varying tangent stiffness that is initially very high, so that accuracy with respect to a mesh without interface element is preserved throughout the model for almost closed interfaces and the change to post peak behavior is less sudden. Fig. 12 illustrates examples of normal and tangential behaviors under pure extension and shear modes, respectively. Black lines represent a linear post-peak behavior ($\beta = \alpha \approx 2$) while non-linear responses are indicated in red. Material damage alters the unloading behavior, which is represented by a straight line passing through the origin. The interface model in this work accounts for a coupling between openings in normal and tangential directions as can be observed in Fig. 13, so that for example fracture energy consumed in the tangential direction affects the response in the normal direction.

6.2.2. Debonding and kinking in a fiber reinforced composite

The non-linear dissipative debonding and kinking of a circular elastic inclusion immersed in an elastic square matrix is approached in two ways: firstly by introducing interface elements with a cohesive interface law, only on their

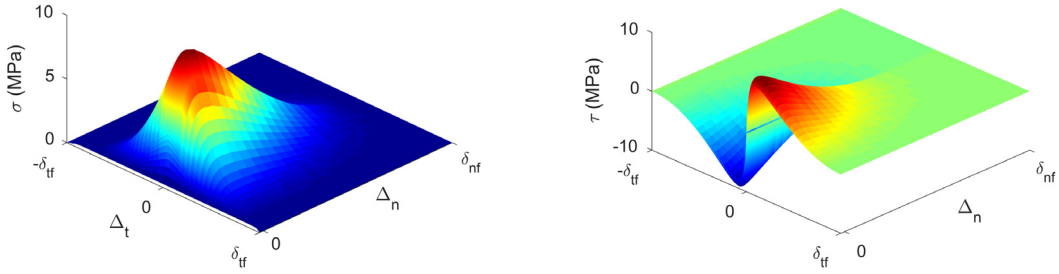

(a) Normal interface stress.

(b) Tangential interface stress.

Fig. 13. Traction separation law with coupling between openings.

Table 3
Data for debonding test.

Bulk			E (MPa)				ν	
Matrix			4 000				0.4	
Fiber			40 000				0.33	
Interface	λ_n	λ_t	ϕ_n	ϕ_t	σ_{max}	τ_{max}	α	β
Matrix–Fiber	10^{-2}	10^{-2}	0.01	0.01	10	10	2	2

intersection (debonding), and secondly by considering non-linear IEs in the interelement boundaries of the matrix as well (kinking). This problem was numerically studied in the literature in the context of discontinuous Galerkin methods [64] as well as augmented Lagrangian [65]. Further details on the debonding and kinking phenomena can be found in [66,67], respectively.

The geometry of the problem, shown in Fig. 14(a), was independently meshed for the inclusion and the matrix. Compatibility of the non conforming meshes was obtained by sharing the nodes on the interface between them (Section 5.1). The problem was solved under the plane strain assumption and material data is reported in Table 3.

For the debonding test, a horizontal displacement $\delta = 2 \cdot 10^{-3}$ mm was imposed and the reaction force computed. The mesh is comprised of 400 elements for the matrix, 100 for the inclusion and 78 IEs. This analysis serves as a benchmark test for the method since interfacial cracks can only appear between matrix and fiber. Results for reaction force and horizontal stress are given in Fig. 14 where dashed lines are provided as a reference. The reaction force shows an almost linear increase until approximately $\delta = 0.35 \cdot 10^{-3}$ mm where the slope decreases slightly until point A, which is a local maximum. As the debonding continues, the reaction force decreases until a local minimum at B, and thereafter shows an asymptotic convergence to the linear relation which is obtained when no inclusion is considered (point C).

For the kinking analysis, a horizontal displacement $\delta = 9 \cdot 10^{-3}$ mm is imposed in several load steps, and again the reaction force is computed. The mesh for this problem is comprised of 2000 and 8000 VEs for the inclusion and the matrix respectively, as well as 412 and 232 97 fiber–matrix and matrix–matrix IEs respectively. Problem data are as indicated in Table 4, noting that elastic parameters for inclusion and matrix are the same as in the debonding problem. As in other cracking analysis using finite and interface elements, the crack path is de-facto predetermined by the discretization, as the cracking can only follow the inter-element boundaries of the mesh between plate and inclusion. Results are presented in Fig. 15 and are qualitatively in good agreement with those obtained in the previously cited works. The horizontal stress at different load steps and at different stages of the kinking process is depicted. The debonding between fiber and matrix appears first due to the lower strength of the interface. Afterwards, the first signs of kinking are observed which keep propagating into the matrix while micro-fractures appear. A state of total failure is reached when the crack covers the entire height of the specimen.

Based on the obtained results, it can be concluded that the proposed approach using VEs yields very similar results to those from other proven methods in the literature, with the advantage of allowing for a less restrictive meshing process and more versatility in element geometry. It is worth mentioning that to overcome the restriction

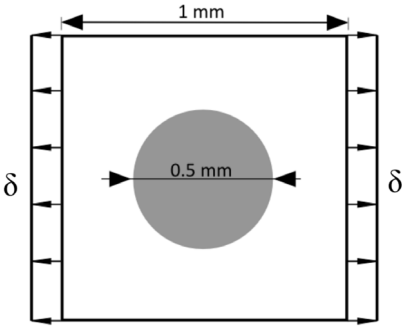

(a) Geometry for the fiber composite debonding and kinking test.

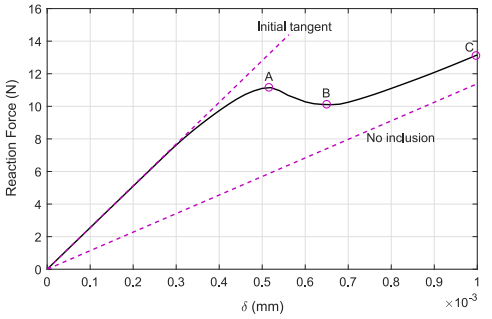

(b) Reaction force–displacement curve.

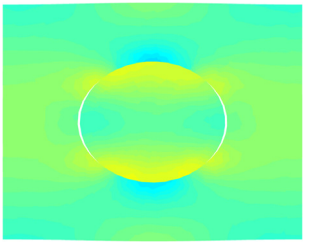

(c) A.

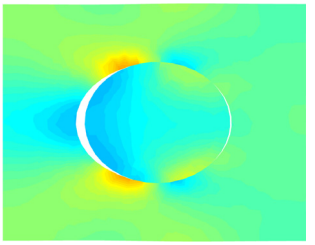

(d) B.

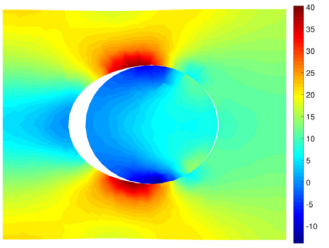

(e) C.

Fig. 14. Reaction force against displacement and horizontal stress σ_x (MPa) with magnification factor = 20 for the debonding test.

Table 4
Data for kinking test.

Interface	λ_n	λ_t	ϕ_n	ϕ_t	σ_{max}	τ_{max}	α	β
Matrix	10^{-2}	10^{-2}	0.20	0.20	30	30	3	3
Matrix–Fiber	10^{-2}	10^{-2}	0.04	0.04	10	10	3	3

of the predefined crack path allowing for arbitrary crack propagation paths, the polygonal VEs can be conveniently subdivided to allow crack propagation through them in case this path actually leads to the maximum post-cracking energy dissipation.

6.2.3. Uniaxial tension

Uniaxial tests of concrete samples are the simplest boundary value problems to be evaluated at the mesoscopic level of observation. For a given aggregate volume ratio of 20%, 3 sample sizes were chosen (10×10, 20×20 and 30×30 in mm) as well as varying element sizes (1 mm^2, $1/2$ mm^2 and $1/3$ mm^2 of average element size), as shown in Fig. 16 along with the final failure state. Aggregates and aggregate-matrix interfaces are shown in red and bright red, while bulk elements and bulk–bulk interfaces are shown in blue and bright blue. Analyses such as this one have an application in modeling RVE (representative volume element) in the framework of multi-scale analysis. Meshing and aggregate selection was performed as explained in Section 5.1 and material parameters are listed in Table 5. The specimens were subjected to a uniform 0.2% vertical strain under plane stress condition, by prescribing horizontal displacement on the left and right boundaries and fixed vertical displacement on the vertical symmetry line. Since the aim in this work is only to show the capabilities of the method, only a sample of all the possible numerical experiments that can be performed by varying material parameters, geometry and meshes are presented. The adopted aggregate volume ratio in practice was $20 \pm 1\%$. Selected results were obtained and compared, as plotted in Fig. 17.

From the results which show the overall specimen behavior up to failure in the tensile test and in terms of both mean axial stress vs. mean axial strain on the one hand (Fig. 17(a)), and mean axial stress vs. axial displacement on the other hand (Fig. 17(b)), the following conclusions can be obtained: post-peak response ductility strongly depends

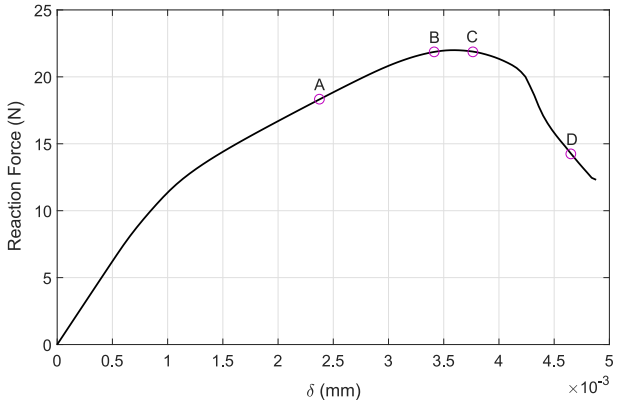

(a) Reaction force vs. displacement.

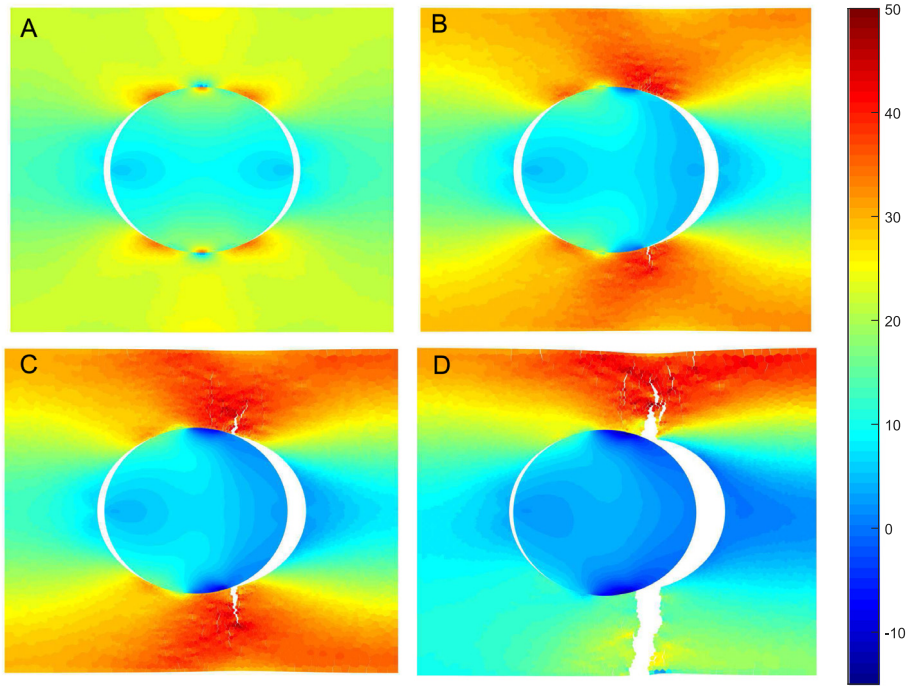

(b) A: Debonding at the interface sets in. B: Kinking initiation. C: Cracking extends to the matrix. D: Complete failure (magnification factor = 20).

Fig. 15. Reaction force against displacement and horizontal stress σ_x (MPa) and for the kinking test.

on the sample size, under conditions of similar aggregate volume ratio and similar maximum aggregate size. This important conclusion, which is demonstrated in the diagrams of Fig. 17 based on both mean axial strains and on axial displacements, are consistent with experimental observations and size effects studies on quasi-brittle materials like concrete. A second relevant conclusion is that the sensitivity of the peak mean axial stress regarding the specimen size is very low and negligible. This is also in agreement with experimental observations published in the scientific literature. Finally, and regarding the failure patterns shown in Fig. 16, the numerical predictions show strong failure localization for all considered sample sizes, which is in line with the well-known concrete failure behavior in the uniaxial tensile test. However, the cracking evolution and distribution in one or two localization bands depend on the aggregate distribution. This is demonstrated with the results in Fig. 18 which correspond to the uniaxial tensile tests on two specimens with the same size (20 × 20 mm) and aggregate volume ratio, but different meshes and

Table 5
Data for the uniaxial and the three point beam tests.

Bulk	E (MPa)	ν	Volume ratio
Matrix	25 000	0.2	0.8
Aggregate	70 000	0.2	0.2

Interface	λ_n	λ_t	ϕ_n	ϕ_t	σ_{max}	τ_{max}	α	β	
Matrix	10^{-2}	10^{-2}	0.06	0.06	6	6	2	2	} Uniaxial
Matrix-Aggregate	10^{-2}	10^{-2}	0.03	0.03	3	3	2	2	
Matrix	10^{-1}	10^{-1}	1	1	6	6	5	5	} Beam
Matrix-Aggregate	10^{-1}	10^{-1}	0.5	0.5	3	3	5	5	

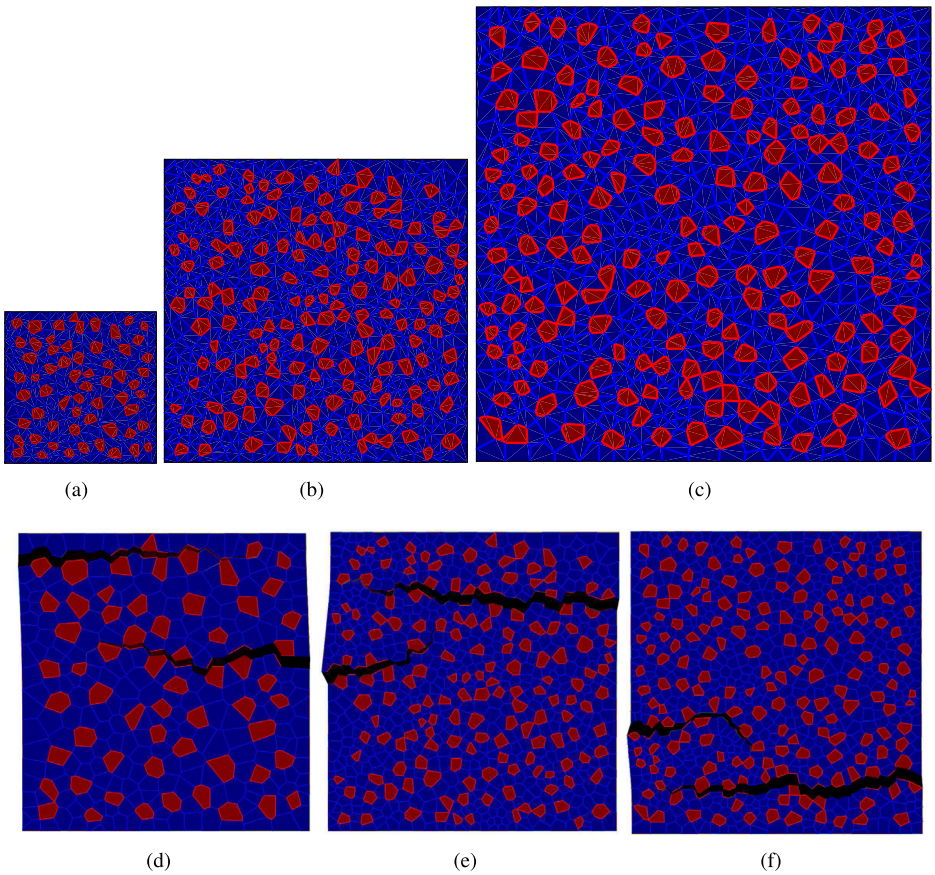

Fig. 16. Upper row: Geometry and meshes for the uniaxial tests. Lower row: Final state at failure (magnification factor = 20 and resized for comparison). (a) and (d) 10 mm × 10 mm −1/3 mm^2 mean element size. (b) and (e) 20 mm × 20 mm −1/2 mm^2 mean element size. (c) and (f) 30 mm × 30 mm −1 mm^2 mean element size. (For interpretation of the references to color in this figure legend, the reader is referred to the web version of this article.)

aggregate distributions. The latter is responsible for the tortuosity of the crack development, and therefore, for the damage concentration in only one or two crack bands. As can be observed in Fig. 18, despite the strong agreement of the pre-peak stiffness/response and peak strength between the two mesoscopic arrangements, the post-peak behavior is strongly influenced by the particular aggregate distribution. These results agree very well with the experimental observation. So, according to the results in this section, the proposed numerical methodology for mesoscopic non-linear and failure analysis of quasi-brittle composites like concrete and cementitious mortars based on VEM and IFs

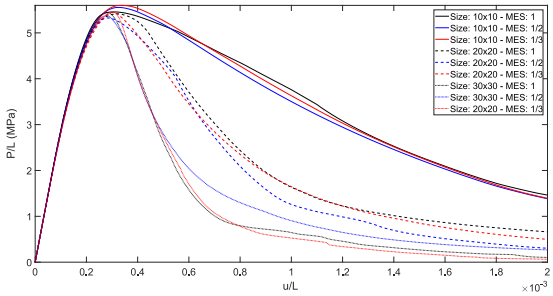

(a) Average force versus normalized displacement.

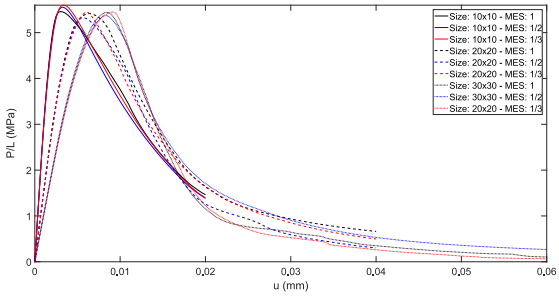

(b) Average force versus displacement.

Fig. 17. Results for the uniaxial test for varying mean element sizes (MES) and sample sizes.

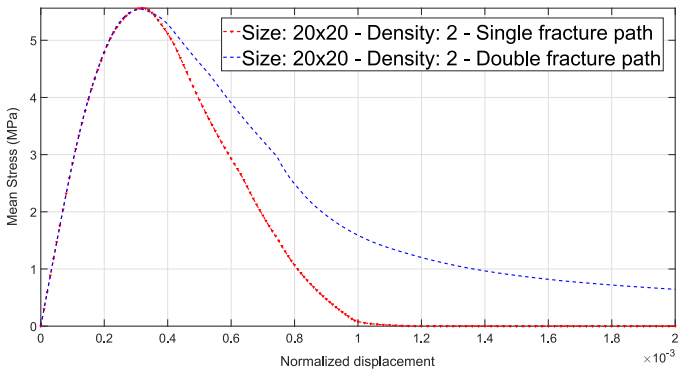

(a)

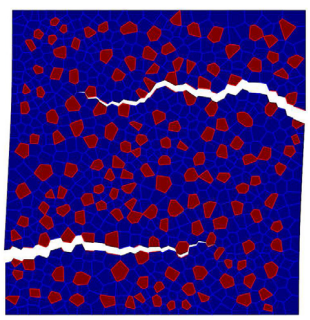

(b) Final state — double path.

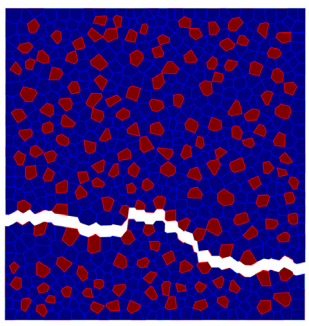

(c) Final state — single path.

Fig. 18. Comparison for a 20 mm × 20 mm specimen with 1/2 mm^2 mean element size with single and double crack paths.

is a very effective and realistic approach which allows details and accurate evaluations of the influence of different material parameters, mixture properties, size and distribution of the involved inclusions, etc.

Further simulations could include pores as a percentage of the total volume of the sample, which can be easily produced by repeating the same procedure for selecting aggregates and either provide them with a negligible stiffness or eliminate them from the mesh altogether. The results presented in this section are of course only a sample aimed at showing the potential of this approach for this type of test. A statistical analysis of the variation in strength due to the randomness of the mesh and aggregate selection out of the scope of this work, but ideas and results in this direction can be found for example in [68].

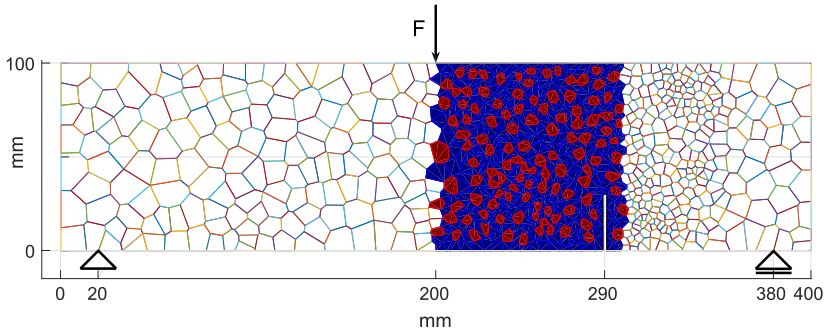

(a) Geometry and boundary conditions.

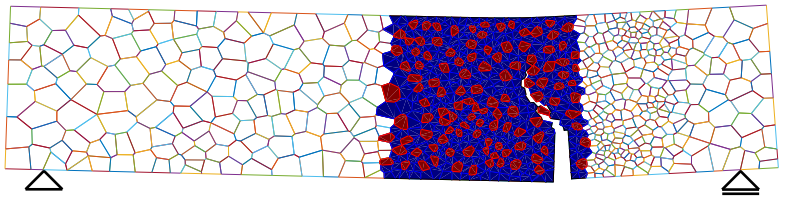

(b) Final State (magnification factor = 5).

Fig. 19. Three point beam test — 920 element mesh.

6.2.4. Analysis of a concrete structural component

The final numerical example deals with the classical three-point bending test on a pre-cracked concrete specimen. Material data is given in Table 5, where a higher fracture energy and a more ductile behavior were imposed in this case as compared to the uniaxial test due to convergence issues arising from the more complex nature of the failure mechanism. Mesh, geometry, loading and boundary conditions for a mesh of 1152 elements for the initial and final states are presented in Fig. 19. Meshing and aggregate selection was again done following the guidelines in Section 5.1.

In the zone where the failure process develops, a mesoscopic discretization with VEM and IEs was performed similar to the one considered in previous subsection, while in the rest of the eccentric three point beam problem, a macroscopic finite element mesh without interfaces was considered. Material properties in the volumetrically discretized portion were obtained as the weighted average between those of the aggregates and the mortar. This problem may serve to assess the feasibility of applying the proposed numerical methodology to a more complex problem related to failure mechanisms under mode II type of fracture. Results of central deflections against applied loading are provided in Fig. 20. Three different randomly generated aggregate distributions (A, B and C) in the mesoscopic zone of the beam were considered for each one of the different and fixed discretizations with 692, 920 and 1152 solid VEs, respectively. As can be observed in Fig. 20, peak force and post-peak behavior in all three different meshes vary with the aggregate distribution. This is reasonable as it affects both the initiation and tortuosity of the cracking process. The resulting failure paths from the numerical analyses agree with experimental observations [69], showing a crack starting at the pre-cracked location which propagates towards the loading point. Despite the involved complexities, the involved numerical tools were able to go through the peak load with stable solutions and without the need of implementing more sophisticated solving algorithms for snap-back and snap-through behaviors, that may present after peak load.

7. Concluding remarks and future developments

In this work a Finite Element methodology based on combining Virtual Elements and Interface Elements was presented for analyzing deformation and failure problems of solid materials and structures at both, macroscopic and mesoscopic levels of observations. Benchmark tests were presented to demonstrate the potentials of this novel approach which may be considered as a reliable alternative and, in some cases, an improvement over standard

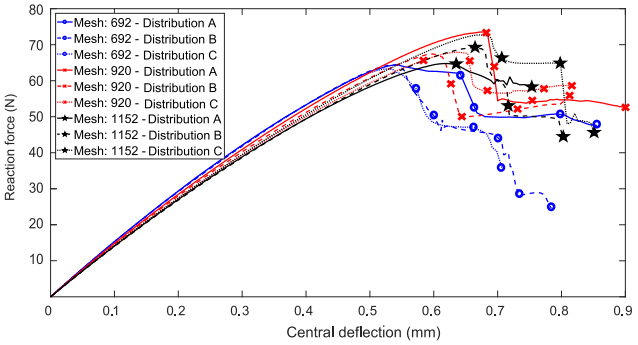

Fig. 20. Three point beam test: results for reaction force against central deflection.

Finite Element methodologies. This is mainly due to the simplifications in the meshing process, particularly in case of mesoscopic analyses where the Virtual Elements strongly facilitate the representation of the geometrical features, leading to more realistic meso-structures. The results showcased here reveal many possible lines of improvements, such as a straightforward extension to 3D simulations with planar interfaces, accounting for higher order approximations of Virtual and Interface Elements, including non-linear dissipative constitutive models in the bulk material, modeling RVE of cementitious mixtures in the framework of multiscale homogenization procedures, introducing a mesh evolution algorithm, etc. The last one is based on one relevant feature, namely, allowing to accommodate meshes of arbitrary polygons and, when the failure criterion is reached in certain element, it can be subdivided along the critical failure directions by simply splitting the element and introducing interfaces along the new solid element borders. Many of the fundamental requirements for this so-called mesh evolution algorithm have been already established in this proposal, making it a feasible strategy for future research. Thus, the presented finite element strategy for failure analyses of materials and structures, based on combinations between Virtual Elements and non-linear dissipative zero-thickness interfaces offers plenty of options for cracking evolution analysis at macroscopic and mesoscopic levels of observations.

Acknowledgments

The second author wishes to acknowledge the Alexander von Humboldt-Foundation for funding his position at the Institute of Construction and Building Materials at TU-Darmstadt under the research grant ITA-1185040-HFST-P (2CENENRGY project).

References

[1] L. Guo, X. Guo, J. Hong, Y. Wang, Constitutive relation of concrete containing meso-structural characteristics, Results Phys. 7 (2017) 1155–1160.
[2] T. Abdullah, L. Liu, Meso-scale phase-field modeling of microstructural evolution in solid oxide fuel cells, J. Electrochem. Soc. 163 (7) (2016) F618–F625.
[3] Y.-G. Fang, B. Li, Multiscale problems and analysis of soil mechanics, Mech. Mater. 103 (2016) 55–67.
[4] M. Romanowicz, A mesoscale study of failure mechanisms in angle-ply laminates under tensile loading, Composites B 90 (2016) 45–57.
[5] A. Caballero, I. Carol, C. López, 3D meso-mechanical analysis of concrete specimens under biaxial loading, Fatigue Fract. Eng. Mater. Struct. 30 (9) (2007) 877–886.
[6] A.E. Idiart, C.M. López, I. Carol, Modeling of drying shrinkage of concrete specimens at the meso-level, Mater. Struct. 44 (2) (2011) 415–435.
[7] S.-M. Kim, R.K.A. Al-Rub, Meso-scale computational modeling of the plastic-damage response of cementitious composites, Cem. Concr. Res. 41 (3) (2011) 339–358.
[8] Y. Rashid, Ultimate strength analysis of prestressed concrete pressure vessels, Nucl. Eng. Des. (ISSN: 0029-5493) 7 (4) (1968) 334–344. http://dx.doi.org/10.1016/0029-5493(68)90066-6. URL http://www.sciencedirect.com/science/article/pii/0029549368900666.
[9] N. Benkemoun, P. Poullain, H. Al Khazraji, M. Choinska, A. Khelidj, Meso-scale investigation of failure in the tensile splitting test: Size effect and fracture energy analysis, Eng. Fract. Mech. 168 (2016) 242–259.
[10] X.-L. Du, L. Jin, J.-Q. Huang, Simulation of meso-fracture process of concrete using the extended finite element method, Chin. J. Comput. Mech. 29 (6) (2012) 940–947.
[11] P. Grassl, D. Grégoire, L.R. Solano, G. Pijaudier-Cabot, Meso-scale modelling of the size effect on the fracture process zone of concrete, Int. J. Solids Struct. 49 (13) (2012) 1818–1827.

[12] G. Cusatis, D. Pelessone, A. Mencarelli, Lattice discrete particle model (LDPM) for failure behavior of concrete. I: Theory, Cem. Concr. Compos. 33 (9) (2011) 881–890.
[13] M. Nitka, J. Tejchman, Modelling of concrete behaviour in uniaxial compression and tension with DEM, Granular Matter 17 (1) (2015) 145–164.
[14] C.M. López, I. Carol, A. Aguado, Meso-structural study of concrete fracture using interface elements. i: numerical model and tensile behavior, Mater. Struct. 41 (3) (2008) 583–599.
[15] A.E. Idiart, C.M. López, I. Carol, Chemo-mechanical analysis of concrete cracking and degradation due to external sulfate attack: A meso-scale model, Cem. Concr. Compos. 33 (3) (2011) 411–423.
[16] L. Beirao da Veiga, G. Manzini, A Virtual Element method with arbitrary regularity, IMA J. Numer. Anal. 34 (2) (2014) 759–781.
[17] A.L. Gain, C. Talischi, G.H. Paulino, On the Vrtual Element method for three-dimensional linear elasticity problems on arbitrary polyhedral meshes, Comput. Methods Appl. Mech. Engrg. 282 (2014) 132–160.
[18] R. Klein, Concrete and Abstract Voronoi Diagrams, in: Lecture Notes in Computer Science, Springer-Verlag, Berlin, 1989.
[19] X. Lei, Contact friction analysis with a simple interface element, Comput. Methods Appl. Mech. Engrg. 190 (15–17) (2001) 1955–1965.
[20] P. Wriggers, Computational Contact Mechanics, Springer Science & Business Media, 2006.
[21] J. Chen, M. Crisfield, A.J. Kinloch, E.P. Busso, F. Matthews, Y. Qiu, Predicting progressive delamination of composite material specimens via interface elements, Mech. Compos. Mater. Struct. 6 (4) (1999) 301–317.
[22] H.A. Baky, U. Ebead, K. Neale, Nonlinear micromechanics-based bond–slip model for FRP/concrete interfaces, Eng. Struct. 39 (2012) 11–23.
[23] D. Xie, S.B. Biggers, Progressive crack growth analysis using interface element based on the virtual crack closure technique, Finite Elem. Anal. Des. 42 (11) (2006) 977–984.
[24] D. Ciancio, I. Carol, M. Cuomo, A method for the calculation of inter-element stresses in 3D, Comput. Methods Appl. Mech. Engrg. 254 (2013) 222–237.
[25] S. Costa Daguiar, A. Modaressi-Farahmand-Razavi, J.A. Dos Santos, F. Lopez-Caballero, Elastoplastic constitutive modelling of soil structure interfaces under monotonic and cyclic loading, Comput. Geotech. 38 (4) (2011) 430–447.
[26] T. Stankowski, K. Runesson, S. Sture, Fracture and slip of interfaces in cementitious composites. I: Characteristics, II: Implementation, ASCE - J. Eng. Mech. 119 (2) (1993) 292–327.
[27] C.M. López, I. Carol, A. Aguado, Meso-structural study of concrete fracture using interface elements. ii: compression, biaxial and Brazilian test, Mater. Struct. 41 (3) (2008) 601–620.
[28] R. Lorefice, G. Etse, I. Carol, Viscoplastic approach for rate-dependent failure analysis of concrete joints and interfaces, Ijss 45 (9) (2008) 2686–2705.
[29] A. Caggiano, G. Etse, E. Martinelli, Zero-thickness interface model formulation for failure behavior of fiber-reinforced cementitious composites, Comput. Struct. 98 (2012) 23–32.
[30] J. Segura, I. Carol, On zero-thickness interface elements for diffusion problems, Int. J. Numer. Anal. Methods Geomech. 28 (9) (2004) 947–962.
[31] J. Liaudat, M. Rodriguez, C. Lopez, I. Carol, Mechanics and Physics of Creep, Shrinkage, and Durability of Concrete: A Tribute to Zdenek P. Bažant: Proceedings of the Ninth International Conference on Creep, Shrinkage, and Durability Mechanics (CONCREEP-9), September 22–25, 2013 Cambridge, Massachusetts, ASCE Publications, 2013.
[32] A. Caggiano, G. Etse, Coupled thermo–mechanical interface model for concrete failure analysis under high temperature, Comput. Methods Appl. Mech. Engrg. 289 (2015) 498–516.
[33] J. Schellekens, R. de Borst, A non-linear finite element approach for the analysis of mode-I free edge delamination in composites, Int. J. Solids Struct. (ISSN: 0020-7683) 30 (9) (1993) 1239–1253. http://dx.doi.org/10.1016/0020-7683(93)90014-X. URL http://www.sciencedirect.com/science/article/pii/002076839390014X.
[34] D. Ciancio, I. Carol, M. Cuomo, On inter-element forces in the fem-displacement formulation, and implications for stress recovery, Internat. J. Numer. Methods Engrg. (ISSN: 1097-0207) 66 (3) (2006) 502–528. http://dx.doi.org/10.1002/nme.1564.
[35] D. Ciancio, I. Carol, G. Castellazzi, Optimal penalty stiffness values of concurrent 2d elastic interface elements leading to accurate stress tractions, Internat. J. Numer. Methods Engrg. (ISSN: 1097-0207) 98 (5) (2014) 344–370. http://dx.doi.org/10.1002/nme.4633.
[36] G. Alfano, M.A. Crisfield, Finite element interface models for the delamination analysis of laminated composites: mechanical and computational issues, Internat. J. Numer. Methods Engrg. (ISSN: 1097-0207) 50 (7) (2001) 1701–1736. http://dx.doi.org/10.1002/nme.93.
[37] Z. Yang, D. Proverbs, A comparative study of numerical solutions to non-linear discrete crack modelling of concrete beams involving sharp snap-back, Eng. Fract. Mech. (ISSN: 0013-7944) 71 (1) (2004) 81–105. http://dx.doi.org/10.1016/S0013-7944(03)00047-X. URL http://www.sciencedirect.com/science/article/pii/S001379440300047X.
[38] F. Brezzi, L. Beirao da Veiga, L.D. Marini, Virtual elements for linear elasticity problems, SIAM J. Numer. Anal. 51 (2) (2013) 794–812. http://dx.doi.org/10.1137/120874746.
[39] L. Beirao da Veiga, C. Lovadina, D. Mora, A Virtual Element Method for elastic and inelastic problems on polytope meshes, Comput. Methods Appl. Mech. Engrg. 295 (2015) 327–346.
[40] E. Artioli, S. de Miranda, C. Lovadina, L. Patruno, A stress/displacement Virtual Element method for plane elasticity problems, Comput. Methods Appl. Mech. Engrg. (ISSN: 0045-7825) 325 (2017) 155–174. http://dx.doi.org/10.1016/j.cma.2017.06.036. URL http://www.sciencedirect.com/science/article/pii/S0045782517302475.
[41] H. Chi, L. Beirao da Veiga, G. Paulino, Some basic formulations of the virtual element method (VEM) for finite deformations, Comput. Methods Appl. Mech. Engrg. (ISSN: 0045-7825) 318 (2017) 148–192. http://dx.doi.org/10.1016/j.cma.2016.12.020. URL http://www.sciencedirect.com/science/article/pii/S0045782516309094.

[42] A.L. Gain, C. Talischi, G.H. Paulino, On the Virtual Element method for three-dimensional linear elasticity problems on arbitrary polyhedral meshes, Comput. Methods Appl. Mech. Engrg. (ISSN: 0045-7825) 282 (2014) 132–160. http://dx.doi.org/10.1016/j.cma.2014.05.005. URL http://www.sciencedirect.com/science/article/pii/S0045782514001509.

[43] O. Andersen, H.M. Nilsen, X. Raynaud, Virtual Element method for geomechanical simulations of reservoir models, Comput. Geosci. (ISSN: 1573-1499) (2017) 1–17. http://dx.doi.org/10.1007/s10596-017-9636-1.

[44] P. Wriggers, W.T. Rust, B.D. Reddy, A virtual element method for contact, Comput. Mech. (ISSN: 1432-0924) 58 (6) (2016) 1039–1050. http://dx.doi.org/10.1007/s00466-016-1331-x.

[45] M.F. Benedetto, S. Berrone, S. Scialò, A globally conforming method for solving flow in discrete fracture networks using the Virtual Element Method, Finite Elem. Anal. Des. 109 (2016) 23–36.

[46] M.F. Benedetto, S. Berrone, A. Borio, S. Pieraccini, S. Scialò, A hybrid mortar virtual element method for discrete fracture network simulations, J. Comput. Phys. (ISSN: 0021-9991) 306 (2016) 148–166. http://dx.doi.org/10.1016/j.jcp.2015.11.034. URL http://www.sciencedirect.com/science/article/pii/S0021999115007743.

[47] L. Beirao da Veiga, F. Brezzi, A. Cangiani, G. Manzini, L.D. Marini, A. Russo, Basic principles of Virtual Element methods, Math. Models Methods Appl. Sci. (2013).

[48] E. Artioli, L. Beirao da Veiga, C. Lovadina, E. Sacco, Arbitrary order 2D virtual elements for polygonal meshes: part I, elastic problem, Comput. Mech. (ISSN: 1432-0924) 60 (3) (2017) 355–377. http://dx.doi.org/10.1007/s00466-017-1404-5.

[49] E. Artioli, L. Beirao da Veiga, C. Lovadina, E. Sacco, Arbitrary order 2D virtual elements for polygonal meshes: part II, inelastic problem, Comput. Mech. (ISSN: 1432-0924) 60 (4) (2017) 643–657. http://dx.doi.org/10.1007/s00466-017-1429-9.

[50] R. Taylor, E. Artioli, VEM for inelastic solids, in: E. Oñate, D. Peric, E. de Souza Neto, M. Chiumenti (Eds.), Computational Methods in Applied Sciences, in: Advances in Computational Plasticity, vol. 46, Springer, Cham, 2018 URL https://link.springer.com/chapter/10.1007/978-3-319-60885-3_18.

[51] J. Oliver, A. Huespe, P. Sanchez, A comparative study on finite elements for capturing strong discontinuities: E-FEM vs X-FEM, Comput. Methods Appl. Mech. Engrg. 195 (37) (2006) 4732–4752.

[52] G. Wells, L. Sluys, A new method for modelling cohesive cracks using finite elements, Internat. J. Numer. Methods Engrg. 50 (12) (2001) 2667–2682.

[53] C. Talischi, G. Paulino, A. Pereira, I. Menezes, PolyMesher: a general-purpose mesh generator for polygonal elements written in Matlab, Struct. Multidiscip. Optim. (ISSN: 1615-147X) 45 (3) (2012). http://dx.doi.org/10.1007/s00158-011-0706-z.

[54] V. Tvergaard, Effect of fibre debonding in a whisker-reinforced metal, Mater. Sci. Eng. A (ISSN: 0921-5093) 125 (2) (1990) 203–213. http://dx.doi.org/10.1016/0921-5093(90)90170-8. URL http://www.sciencedirect.com/science/article/pii/0921509390901708.

[55] K. Park, G.H. Paulino, J.R. Roesler, A unified potential-based cohesive model of mixed-mode fracture, J. Mech. Phys. Solids 57 (6) (2009) 891–908.

[56] T. Belytschko, W.K. Liu, B. Moran, K. Elkhodary, Nonlinear Finite Elements for Continua and Structures, second ed., Wiley, 2014.

[57] E. Artioli, S. Marfia, E. Sacco, Virtual element technique for computational homogenization problems, in: Proceedings of AIMETA 2017 XXIII Conference The Italian Association of Theoretical and Applied Mechanics, 2018.

[58] E. Artioli, Asymptotic homogenization of fibre-reinforced composites: a virtual element method approach, Meccanica (ISSN: 1572-9648) (2018). http://dx.doi.org/10.1007/s11012-018-0818-2.

[59] X. An, G. Ma, Y. Cai, H. Zhu, A new way to treat material discontinuities in the numerical manifold method, Comput. Methods Appl. Mech. Engrg. (ISSN: 0045-7825) 200 (47–48) (2011) 3296–3308. http://dx.doi.org/10.1016/j.cma.2011.08.004. URL http://www.sciencedirect.com/science/article/pii/S0045782511002593.

[60] M. Paggi, P. Wriggers, Node-to-segment and node-to-surface interface finite elements for fracture mechanics, Comput. Methods Appl. Mech. Engrg. (ISSN: 0045-7825) 300 (2016) 540–560. http://dx.doi.org/10.1016/j.cma.2015.11.023. URL http://www.sciencedirect.com/science/article/pii/S0045782515003837.

[61] K. Park, G.H. Paulino, Computational implementation of the PPR potential-based cohesive model in ABAQUS: Educational perspective, Eng. Fract. Mech. (ISSN: 0013-7944) 93 (2012) 239–262. http://dx.doi.org/10.1016/j.engfracmech.2012.02.007. URL http://www.sciencedirect.com/science/article/pii/S0013794412000690.

[62] F. Parrinello, G. Marannano, G. Borino, A thermodynamically consistent cohesive-frictional interface model for mixed mode delamination, Eng. Fract. Mech. (ISSN: 0013-7944) 153 (2016) 61–79. http://dx.doi.org/10.1016/j.engfracmech.2015.12.001. URL http://www.sciencedirect.com/science/article/pii/S0013794415006736.

[63] F. Freddi, E. Sacco, R. Serpieri, An enriched damage-frictional cohesive-zone model incorporating stress multi-axiality, Meccanica (ISSN: 1572-9648) (2017). http://dx.doi.org/10.1007/s11012-017-0777-z.

[64] V.P. Nguyen, Discontinuous galerkin/extrinsic cohesive zone modeling: Implementation caveats and applications in computational fracture mechanics, Eng. Fract. Mech. (ISSN: 0013-7944) 128 (2014) 37–68. http://dx.doi.org/10.1016/j.engfracmech.2014.07.003. URL http://www.sciencedirect.com/science/article/pii/S0013794414002136.

[65] N.A. Labanda, S.M. Giusti, B.M. Luccioni, Meso-scale fracture simulation using an augmented lagrangian approach, Int. J. Damage Mech. 27 (1) (2018) 138–175 URL https://doi.org/10.1177/1056789516671092.

[66] I. Garca, M. Paggi, V. Manti, Fiber-size effects on the onset of fibermatrix debonding under transverse tension: A comparison between cohesive zone and finite fracture mechanics models, Eng. Fract. Mech. (ISSN: 0013-7944) 115 (2014) 96–110. http://dx.doi.org/10.1016/j.engfracmech.2013.10.014. URL http://www.sciencedirect.com/science/article/pii/S0013794413003408.

[67] F. París, E. Correa, V. Mantič, Kinking of transversal interface cracks between fiber and matrix, J. Appl. Mech. 74 (4) (2007) 703–716.

[68] X. Wang, Z. Yang, A.P. Jivkov, Monte Carlo simulations of mesoscale fracture of concrete with random aggregates and pores: a size effect study, Constr. Build. Mater. (ISSN: 0950-0618) 80 (2015) 262–272. http://dx.doi.org/10.1016/j.conbuildmat.2015.02.002. URL http://www.sciencedirect.com/science/article/pii/S0950061815001154.

[69] A. Carpinteri, R. Brighenti, Fracture behaviour of plain and fiber-reinforced concrete with different water content under mixed mode loading, Mater. Des. (ISSN: 0261-3069) 31 (4) (2010) 2032–2042. http://dx.doi.org/10.1016/j.matdes.2009.10.021. URL http://www.sciencedirect.com/science/article/pii/S0261306909005743. Design of Nanomaterials and Nanostructures.